Energy Storage Materials 61 (2023) 102853

Contents lists available at ScienceDirect

Energy Storage Materials

journal homepage: www.elsevier.com/locate/ensm

High-entropy two-dimensional metal phosphorus trichalcogenides boost high-performance potassium ion storage devices via electrochemical reconstruction

Po-Wen Chien, Che-Bin Chang, Hsing-Yu Tuan *

Department of Chemical Engineering, National Tsing Hua University, Hsinchu 30013, Taiwan

ARTICLE INFO

Keywords:
Potassium ion
High-entropy
2D material
Battery
Hybrid capacitor

ABSTRACT

We investigate the influence of configurational entropy on the cycling performance of 2D metal phosphorus trichalcogenides (MPS_3) when utilized as anodes in potassium-ion devices. High yield, two-dimensional high-entropy $CoVMnFeZnPS_3$ ($HEPS_3$) with thickness ranging from 6 to 10 nm was synthesized via a vacuum solid-state method. $HEPS_3$ enables efficient potassium-ion transport and intercalation at the interface of electrodes, thanks to the high-entropy effects arising from the interaction of various metal ions on the K^+ binding energy. $HEPS_3$ potassium-ion anodes outperform their medium-entropy ($CoMnFePS_3$ (ME_3PS_3) and $CoMnFeZnPS_3$ (ME_4PS_3)), $CoFePS_3$ (LE_2PS_3), and $FePS_3$ ($LEPS_3$) counterparts, exhibiting a high reversible capacity of 524 mAh g^{-1}, impressive high-rate capability up to 10 A g^{-1}, and exceptional cycling stability over 1000 cycles. Our findings indicate that the electrochemical reconstruction of $HEPS_3$ during cycling is crucial for achieving high-performance potassium-ion batteries. In situ-formed metal alloy layers act as catalysts, offering not only suitable adsorption energy to prevent the shuttle effect but also promoting the complete conversion of polysulfides. Furthermore, cations uniformly dispersed across the 2D plane create a "lattice distortion effect," imparting the structure with high mechanical stability and allowing for even distribution of internal stress generated in the electrode during the K^+ insertion/extraction process, which in turn suppresses electrode pulverization and prevents the aggregation of $MPCh_3$ layers. This work proposes a novel strategy for significantly enhancing potassium-ion storage performance through the electrochemical activation of high-entropy layered metal phosphides, thus opening a new horizon of 2D material design principle in energy storage devices.

1. Introduction

Potassium-ion batteries (PIBs) are considered as a promising substitute for lithium-ion batteries in large-scale energy storage due to their higher abundance [1], ionic conductivity, ion mobility, cell voltage, and energy density [2–5]. However, the larger ionic radius of K^+ contributes to irreversible electrode degradation during potassiation/depotassiation, diminishing specific capacity and rate performance [6,7]. Conversion-type anodes, compared to intercalation-type and alloy-type anodes [8–10], are more common, facilitating multiple redox processes and higher theoretical capacity for rechargeable batteries [11]. Some conversion-type anodes can form new structures during cycling, reducing drastic volume changes and boosting electron and ion transport for reversible ion storage [12]. For instance, FeF_2 forms a Fe network during lithiation, enhancing material's specific surface area and electron conduction, and enabling a reversible LiF reaction [13]. Consequently, development of suitable conversion-type anode materials that can reversibly accommodate large-sized K^+ is considered more promising.

To achieve efficient K^+ storage, two-dimensional (2D) conversion-type materials made up of layered compounds are the ideal choice. The unique characteristics of 2D nanomaterials make them highly suitable as advanced electrode materials for potassium-ion batteries. First, their special two-dimensional structure allows for even distribution of internal stress generated during K^+ insertion/extraction, effectively relieving accumulated mechanical stress, preventing electrode pulverization, and further enhancing reversible potassium storage performance. This, in turn, contributes to better long-term cycle performance of the battery [14]. Second, 2D nanomaterials have tunable interlayer spacing and high electrical conductivity, which helps provide

* Corresponding author.
E-mail address: hytuan@che.nthu.edu.tw (H.-Y. Tuan).

https://doi.org/10.1016/j.ensm.2023.102853
Received 7 April 2023; Received in revised form 25 May 2023; Accepted 12 June 2023
Available online 22 June 2023

fast ion transport channels and potential reaction sites, significantly reducing the diffusion distance of K^+, promoting ion intercalation and electron transfer, and diffusion kinetic [15]. Third, the large surface area of 2D materials ensures a larger contact area between the material and electrolytes, allowing for better charge distribution. Additionally, the highly exposed atoms on the surface endow the material with more active sites for electrochemical reactions, which is beneficial for ion adsorption and improving the storage capacity of capacitor-type electrode materials [16]. 2D metal phosphorus trichalcogenides ($MPCh_3$, where M = V, Mn, Fe, Co, Ni, Zn, etc., Ch = S, Se) are expected to become a new generation of energy storage materials due to their unique structure, tunable composition, high surface activity, and high mobility [17]. In particular, the special structure of the metal layer surrounded by sulfur and phosphorus facilitates the intercalation of alkali metal ions. However, $MPCh_3$ compounds for PIB_S exhibit limited specific capacity and cycle performance. One challenging is that, due to van der Waals attraction, 2D nanosheets are prone to stack together, which reduces surface area and restricts ion diffusion, ultimately hindering the rapid transport of electrons and ions and seriously compromising the electrochemical performance [18,19].

In recent years, high-entropy materials (HEMs) have emerged as a new concept in the field of materials science and have found applications in various fields such as pharmaceuticals [20], catalytic systems [21], thermoelectric applications [22], and electrochemical energy storage [23]. Unlike traditional materials, high-entropy materials possess four unique effects due to their composition of five or more kinds of metals with similar atomic ratios: the high-entropy effect, sluggish diffusion effect, lattice distortion effect, and "cocktail" effect. The single-phase structure formed by the lattice distortion effect is particularly beneficial to the catalysis of the energy conversion process due to the strong synergistic effects among the individual elements, which can form suitable reaction sites more supportive of gas absorption [24]. Recently, Wang et al. demonstrated that high-entropy metal phosphorus trichalcogenides (such as $Co_{0.6}(VMnNiZn)_{0.4}PS_3$) with optimized S sites on the edge and P sites on the basal plane provide more active sites than ternary metal phosphorus trichalcogenides (such as $CoPS_3$) [25]. High-entropy materials also exhibit attractive properties in the field of electrochemical energy storage. It has been shown that increasing the configurational entropy (compositional disorder) can positively affect battery performance and stability. A unique entropy-stabilized conversion mechanism for rock-salt high-entropy oxides (HEOs) as a lithium storage anode is proposed, resulting in enhanced cycle stability and Coulombic efficiency [26]. Additionally, Zhao et al. studied the high-entropy material HE-CMFSGS with a tetragonal structure as a conversion-type anode for sodium storage and confirmed that the high-entropy configuration can effectively suppress the continuous aggregation of Sn nanocrystalline and increase the interfacial contact between M^0 and Na_2S, enabling highly reversible conversion reactions [27]. Despite some challenges, high-entropy materials have shown great potential for various applications, and further research in this field is highly encouraged.

In this study, we present the concept of high entropy in two-dimensional metal phosphorus trisulfide (MPS_3) systems for use as anode materials in potassium-ion storage devices. Through the high-entropy effects generated by the interplay of multiple metal ions on K^+ binding energy, the $CoVMnFeZnPS_3$ ($HEPS_3$) system enables potassium-ion transport and intercalation. Furthermore, we discover that high-entropy materials undergo electrochemical reorganization during cycling, leading to the formation of novel sheet-like structures through metal alloy precipitation. These structures also serve as catalysts, fostering the transformation of polysulfides and expediting electron transport. The inherent mechanical stability of these structures effectively reduces the accumulated mechanical stress during the continuous insertion/extraction of K^+, thereby preventing electrode pulverization and ongoing disruption of the solid electrolyte interface (SEI) film.

2. Experimental section

2.1. Materials

The iron powder (98%) was purchased from J.T. Bakers. The red phosphorus powder (97%), cobalt powder (99.999%), vanadium powder (99.999%), zinc powder (99.999%), potassium metal (chunks in mineral oil, 98%), dimethyl carbonate (DMC, anhydrous 99%), potassium hexacyanoferrate(II) trihydrate ($K_4Fe(CN)_6{\cdot}3H_2O$, 99.5%), and Sodium carboxymethyl cellulose (NaCMC, average M_w~700,000) were purchased from Sigma-Aldrich. Manganese powder (99.3%) and sulfur powder (>99% purities) were purchased from Alfa-Aesar. Coin-type cell CR2032 and Super-P were purchased from shining energy. Potassium bis (fluorosulfonyl)imide (KFSI, 97%) was purchased from Combi-Blocks. Copper foil were purchased from Chang-Chun group. Glass fiber was purchased from Advantec. All chemicals were of analytical grade and were used as received without purification, unless otherwise specified.

2.2. Synthesis of bulk $HEPS_3$

Bulk $HEPS_3$ was prepared by traditional solid-state reaction with their nominal composition powders (total mass of 200 mg). The elemental powders were sealed into quartz tubes under a dynamic vacuum of 3.5×10^{-2} Pa. The sealed samples were heated in a muffle furnace from room temperature to 610 °C with a heating rate of 1 °C min^{-1}. After it was maintained at 610 °C for 48 h, the furnace was cooled to room temperature naturally, and a series of bulk samples were obtained.

2.3. Synthesis of $MPCH_3$ NS with different entropy

The preparation of $MPCH_3$ (ME_4PS_3, ME_3PS_3, LE_2PS_3 and $LEPS_3$) with different entropy is the same as mentioned above except the amounts of metal powder used.

2.4. Synthesis of $HEPS_3$@G composites

The $HEPS_3$@G composites were synthesized via high energy mechanical milling (HEMM). $HEPS_3$ and graphite (the mass ratio was 2:1) were placed into a stainless-steel jar with stainless-steel balls and sealed inside an argon-filled glovebox. The mass ratio of ball to powder is about 180:1. Finally, the mixture was ball milled for 24 h.

2.5. Synthesis of $MPCH_3$@G composites with different entropy

The preparation of $MPCH_3$@G (ME_4PS_3@G, ME_3PS_3@G, LE_2PS_3@G and $LEPS_3$@G) with different entropy followed same protocols mentioned above.

2.6. Synthesis of Prussian blue (PB)

In a typical synthesis process, 5 mmol of $FeCl_2{\cdot}4H_2O$ was dissolved in 100 ml of DI water to be solution A, while 5 mmol of $K_4Fe(CN)_6{\cdot}3H_2O$, 10 mmol potassium citrate, and excess potassium chloride were dissolved in DI water to form solution B. Then, solution A was slowly added into solution B by precipitation method, and waited for a six-hour suspension. After that, the product was centrifugated and washed for three times with a mixture of DI water, and finally dried at 80 °C in a CVD for 2 h.

2.7. Materials characterizations

The morphologies of the obtained samples were investigated using scanning electron microscopy (SEM, Hitachi SU8010) equipped with energy-dispersive X-ray spectroscopy (EDS) detector. Transmission electron microscopy (TEM) (JEOL, JEM-ARM200FTH, serviced

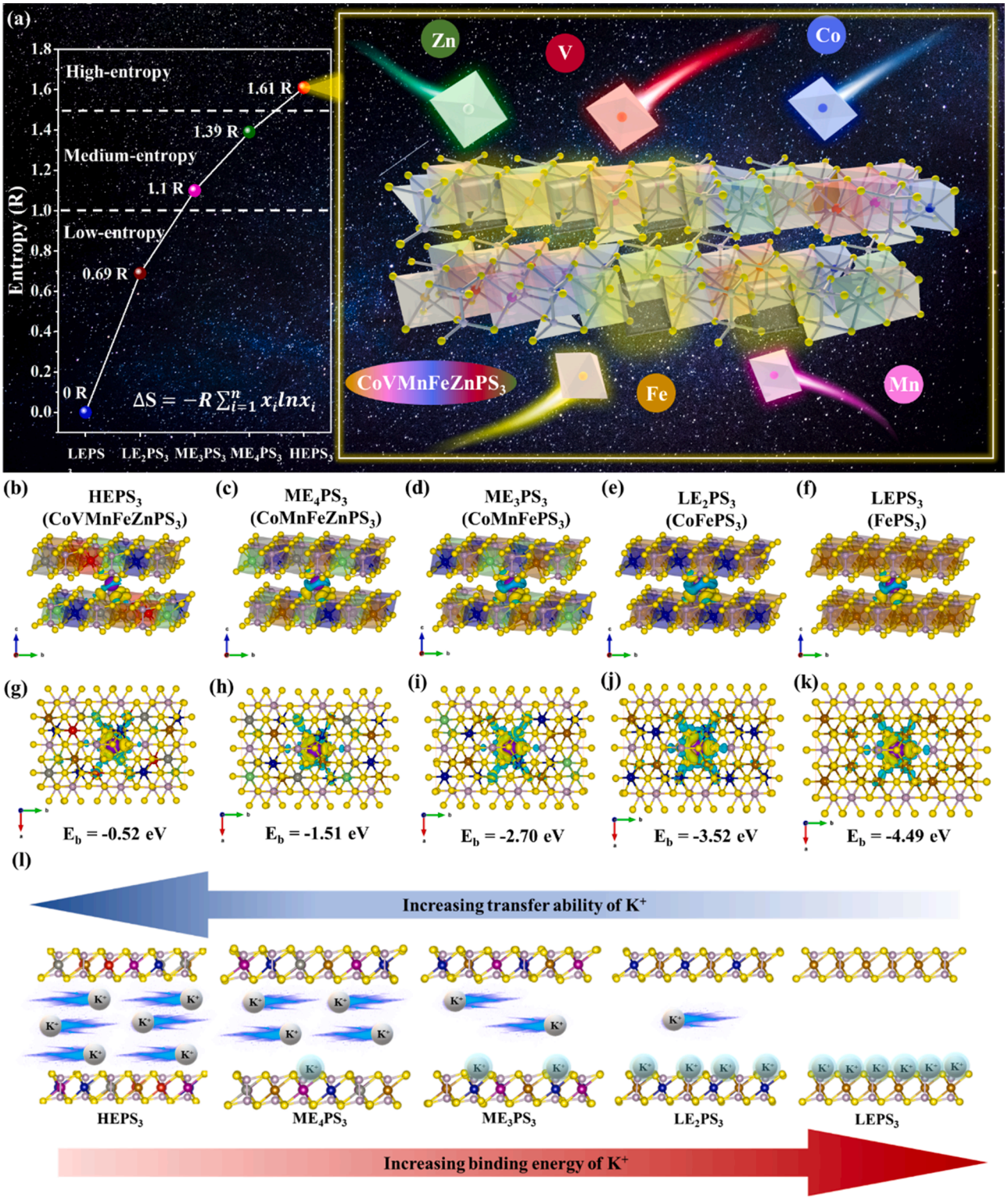

Fig. 1. (a) Calculated configurational entropy and (b-k) charge density differences of K^+ adsorbed on $HEPS_3$, ME_4PS_3, ME_3PS_3, LE_2PS_3 and $LEPS_3$ for side view and top view. (l) Scheme illustration of the transfer ability of two-dimensional metal phosphorus trichalcogenides with different configurational entropy.

provided by NTHU) with an accelerating voltage of 200 kV for investigating structural analysis including morphology, crystal lattice spacing, and selected-area electron diffraction (SAED). The structural evolution and composition were identified using X-ray diffraction (Bruker, D8 ADVANCE) with Cu-Kα radiation (λ = 1.54 Å) and the oxidation states of the samples were characterized by high-resolution Xray photoelectron spectrometer (XPS, ULVAC-PH, PHI QuanteraII, NTHU). All the spectra obtained from XPS analysis were first calibrated by referencing the standard binding energy of C 1 s (284.8 eV), followed by the curve fitting using the software of XPSPEAK VER. 4.1. Thermogravimetric analysis was performed using a thermogravimetric analyzer (TA, Q50) in the atmosphere with a temperature ramp rate of 10 °C min^{-1} and a temperature range of 25–800 °C. Raman spectroscopy was performed using a Micro Raman Identify Dual (MRID). TOF-SIMS data were collected on

a TOF-SIMS V spectrometer (ION-TOF GmbH). 1 keV Cs^+ (negative mode) ion beam was used for the sputtering with a typical area of 120 μm × 120 μm. AFM study was performed by BRUKER Dimension Icon. UV–vis diffuse reflectance spectra were taken using a JASCO V-670 spectrophotometer equipped with an integrating sphere.

2.8. Electrochemical measurements

These electrodes were prepared by mixing the active material ($HEPS_3$@G 70%), super-P carbon black (20%), and NaCMC (10%) in DI water to form a uniform slurry. The homogeneous slurry was coated onto the copper foil and dried under vacuum at 80 °C for 1 h in a furnace to remove the residual solvent. The mass loading of active material in $HEPS_3$@G are 0.7∼1.0 mg cm^{-2}. For electrochemical test, the half cells were assembled with the potassium foil as the counter electrode, a solution of 1 M potassium bis(fluorosulfonyl)imide (KFSI, Chemical Block, 97%) in dimethyl carbonate (DMC, anhydrous 99.5%) as electrolyte, and glass fiber filters (Advantec.) as a separator. CR2032 coin cells were assembled in an argon-filled glove box with both the moisture and the oxygen content bellow 1 ppm (M. Braun UNILAB). Galvanostatic charge/discharge tests were evaluated by NEWARE CT-4000 battery measurement system from 0.01 to 3.0 V vs. K^+/K. Galvanostatic intermittent titration technique (GITT) were evaluated by Maccor Series 4000 battery test system. Cyclic voltammetry (CV) and electrochemical impedance spectroscopy (EIS) curves were obtained on Bio-Logic-Science Instruments, VMP3 workstation.

2.9. Calculation details

All the spin-polarized density functional theory (DFT) calculations were carried out using Vienna Ab-initio Simulation Package (VASP). The exchange and correlation energies were determined with the Perdew, Burke, and Ernzerhof (PBE) functional within the generalized gradient approximation (GGA). The electron-ion interactions were described by using projector augmented wave (PAW) method. The DFT-D3 dispersion correction with Becke-Jonson damping was used to consider the van der Waals interaction. According to our careful convergence tests, the cutoff energy of plane-wave basis was 400 eV. The self-consistence-field convergence criterion was set to 10^{-4} eV, and the atomic positions were optimized with the convergence criterion of 0.02 eV/Å. The Brillouin zone was sampled by a Monkhorst-Pack K-point mesh with a grid of 3 × 2 × 1. A thermal Gaussian smearing of 0.05 eV to the orbital occupation was applied to speed up electronic convergence. The 2-layer 3 × 1 supercell of $FePS_3$ slab was used to build all the calculation models, and an additional vacuum layer of 15 Å was added to the model to avoid the artificial interaction effect between the slab and their mirror images. The corresponding proportion of Fe atoms were replaced by Co, V, Mn, and Zn, respectively, to construct “high-entropy” models. The geometry structures and charge density difference plots were illustrated with VESTA software.

2.10. Potassium-ion full cell of $HEPS_3$@G//PB

The CR2032 potassium-ion coin type full cell was assembled by setting the cathode-to-anode overall surface charge ratio to be 1. Before full cell assembly, both anode and cathode were preactivated for 23 cycles and discharge to 0.01 V followed by constant voltage process to maintain the state of the electrodes. Then, 1 M KFSI in DMC was applied as electrolyte and the working window of the full cell was set between 1 V ∼ 3.8 V.

2.11. Potassium-ion hybrid capacitor of $HEPS_3$@G//AC

The potassium-ion hybrid capacitor was assembled by using $HEPS_3$@G for anode and active carbon for cathode, with an overall mass ratio to be 1. Before the hybrid capacitor assembly, the anode was preactivated for 23 cycles and discharge to 0.01 V. Afterwards, we used 1 M KFSI in DMC as the electrolyte and set the working window of the hybrid capacitor between 0.01 V ∼ 3.8 V.

3. Results and discussion

The high entropy engineering was introduced in two-dimensional metal phosphorus trichalcogenide system, ($MPCh_3$, where M = V, Mn, Fe, Co, Ni, Zn, etc., Ch = S, Se). To evaluate the influence of configurational entropy to electrochemical performance, different entropy materials were prepared by a vacuum solid-state method [28], including $LEPS_3$, LE_2PS_3, $CoMnFePS_3$ (ME_3PS_3), $CoMnFeZnPS_3$ (ME_4PS_3) and $CoVMnFeZnPS_3$ ($HEPS_3$). There are two main definitions of high-entropy alloys, namely, composition-based and configuration-based entropy. In the former definition, high-entropy alloys refer to alloys containing at least 5 main elements and the atomic percentage of each element is in the range of 5% to 35%. If there are trace elements, the atomic percentage of each element should be less than 5%. For the second definition, high-entropy alloys are defined as alloys whose configuration entropy is greater than 1.5R in a random state, whether single-phase or multi-phase at room temperature. Therefore, materials with $\Delta S \geqq 1.5$ R are classified as high-entropy, while materials with 1.0 R $\leqq \Delta S \leqq$ 1.5 R and ΔS <1.0 R are classified as medium-entropy and low-entropy [24], respectively, calculated by the formula of $\Delta S = -R\sum_{i=1}^{n} x_i ln x_i$, where R is the ideal gas constant, and x_i represents the mole fraction of the i th component. From the above classification and calculation, it can be concluded that among the five synthesized two-dimensional metal phosphorus trichalcogenides. The configuration entropy of $LEPS_3$ and LE_2PS_3 are 0 R and 0.69 R respectively, which are classified as low entropy; ME_3PS_3 and ME_4PS_3 with configurational entropy of 1.1R and 1.39R, respectively, which are classified in the medium entropy. Finally, the calculated configurational entropy of $HEPS_3$ is 1.61 R, which is classified as high entropy. The right side of Fig. 1b illustrate the sturcutue of high entropy metal phosphorus trichalcogenides in the configuration entropy mainly contributed by Co, V, Mn, Fe, and Zn rather than P and S. To further advance our understanding of the impact of configuration entropy, DFT calculations were performed in VASP [29], in which 2 layers of 3 × 2 × 1 $FePS_3$ slab supercells were used to construct all calculation models, and an additional 15 Å vacuum layer to avoid artifactual interaction effects between the slab and its mirror image. Corresponding proportions of Fe atoms were replaced by Co, V, Mn and Zn, thereby constructing a "high entropy" model. The calculation results are shown in Table S1 in the supporting information. The binding energy of high-entropy materials to K^+ is the weakest (Fig. 1b), such weak binding energy is conducive to the migration of K^+ in high-entropy materials, making them uniformly distributed inside the material. In addition, if the binding energy of the material to K^+ is relatively weak, it means that the potential well of K^+ at the current position is relatively shallow, which is more conducive to the migration of K^+. It can be further regarded as an indirect evidence that K^+ have the lowest diffusion energy barrier in high-entropy materials. Since K^+ must first leave the corresponding site during the diffusion process, and then migrate to the adjacent position, the weaker the binding energy is, the more conducive it is to diffuse, corresponding to a lower diffusion energy barrier. Therefore, the high-entropy two-dimensional layered structure $HEPS_3$ could be beneficial to the rapid transfer of electrons and K^+ [30]. Although the $HEPS_3$ electrode will not return to the $HEPS_3$ phase after the initial reaction, the rapid transfer of K^+ in the initial reaction will facilitate the complete electrochemical reconstruction reaction, so the diffusion behavior of K^+ in the initial reaction is emphasized. In short, we know that K^+ migrate most easily in the $HEPS_3$ with the highest configurational entropy through theoretical calculations, so we have follow-up experimental ideas. These findings provide an avenue for designing high-performance K^+ energy storage systems based on high-entropy 2D materials.

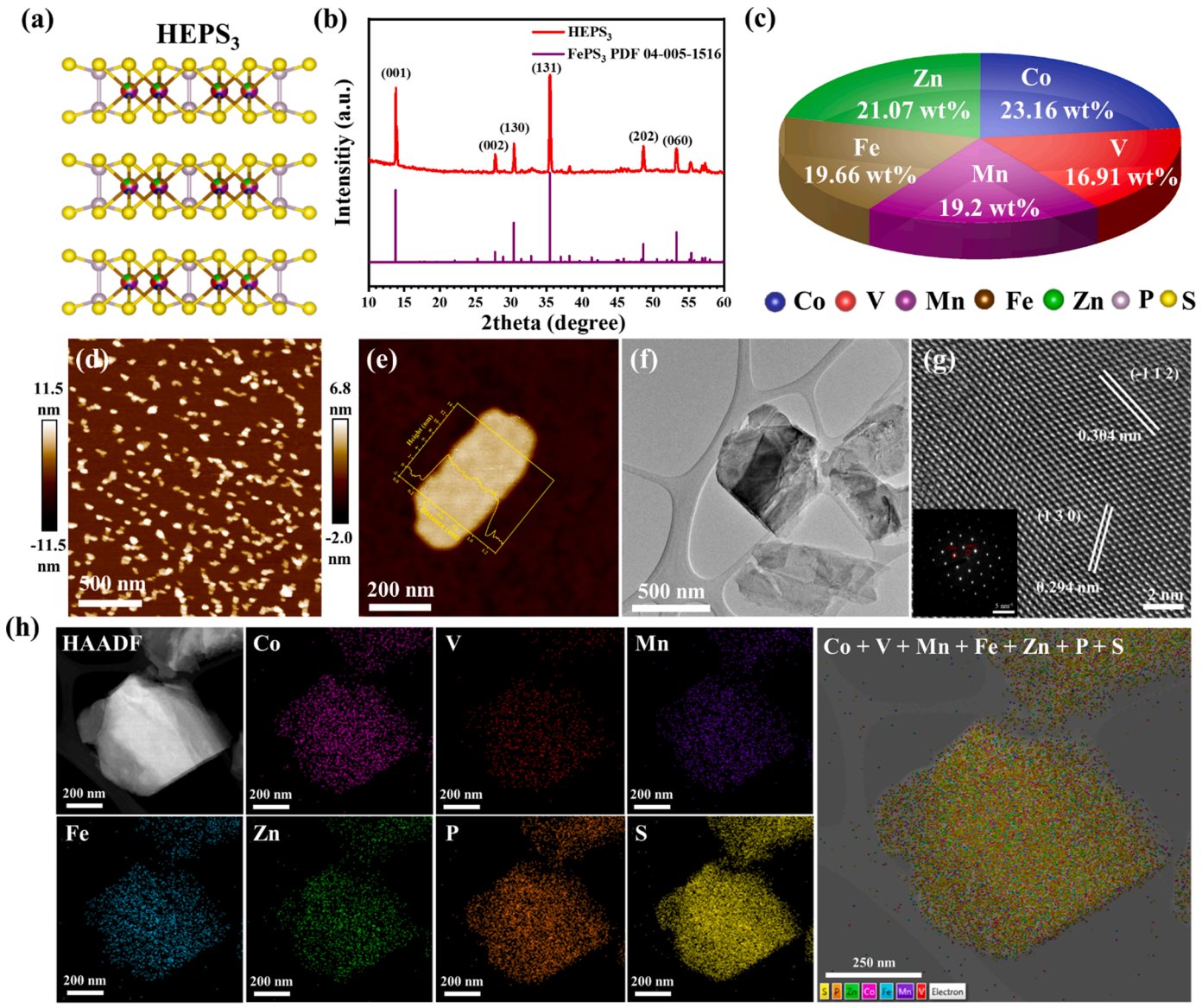

Fig. 2. (a) Crystal structure of $HEPS_3$ nanoflakes. (b) XRD pattern of $HEPS_3$ nanoflakes. (c) Chemical composition of $HEPS_3$ nanoflakes from ICP-OES analysis. (d-e) AFM images, (f) TEM image, and (g) HRTEM image of as-prepared $HEPS_3$ nanoflakes. Insets present the SAED pattern. (h) EDS mapping images of $HEPS_3$ and corresponding elements of Co, V, Mn, Fe, Zn, P and S.

The preparation of $HEPS_3$ was carried out using a conventional solid-state method. Initially, high-purity elements of Co, V, Mn, Fe, Zn, P, and S were sealed in a vacuum quartz tube. Subsequently, the tube was placed in a furnace at 610 °C for 48 h with a heating rate of 1 °C per minute, and the layered crystal product of $HEPS_3$ was finally collected (Fig. S1). The structure of the $HEPS_3$ sample is depicted in Fig. 2a, where metal atoms are sandwiched between two atomic layers of S and P. Co, V, Mn, Fe, and Zn transition metal atoms share the same intermediate metal position. The powder X-ray diffraction pattern (PXRD) of the $HEPS_3$ nanosheet is shown in Fig. 2b. The enthalpy of formation is much lower than the configurational entropy in high-entropy $MPCh_3$. Hence, the pure-phase monoclinic structure (C2/m) with high crystallinity inherited from this component. The same situation can also be found at other transition metal trichalcogenides with different configurational entropy (Fig. S2). Taking $HEPS_3$ and $FePS_3$ as representative examples, all the diffraction peaks of $HEPS_3$ are well matched with monoclinic $FePS_3$ (JCPDS No. 04–005–1516), indicating that there is no impurity phase (Fig. 2b). The main diffraction peaks at 14°, 28°, 30°, 35°, 49°, and 53° correspond to (001), (002), (130), (131), (202), and (060) crystal faces, respectively. This result shows that $HEPS_3$ sample is classified as a single-phase monoclinic structure (C2/m), and there are no additional diffraction peaks indicating that it is a pure phase rather than a mixture. However, the composition ratio of the metal cations in the pure phase cannot be known from the XRD pattern. Therefore, to determine the composition of each transition metal atom in high-entropy transition metal trichalcogenides nanosheets, inductively coupled plasma-optical emission spectroscopy (ICP-OES) was performed, and the results are shown in Fig. 2c. The weight percentage of Co atoms was the highest at 23.16 wt%, while V atoms had the least weight percentage of 16.91 wt %. The proportions of the other metal atoms, such as Fe, Mn, and Zn, did not differ much [31]. Thus, the ratio of the real composition of the five metals was confirmed to be close to 1:1:1:1:1. Additionally, the atomic ratios of other transition metal trichalcogenides with different configurational entropy are also shown in Table S2. To determine the thickness of $HEPS_3$ nanoflakes, atomic force microscopy (AFM) was performed, as shown in Fig. 2d. The prepared high-entropy nanosheets were uniformly dispersed on the substrate, and the thickness ranges from 6 to 10 nm. Fig. 2e is an AFM image of a single high-entropy nanosheet, showing

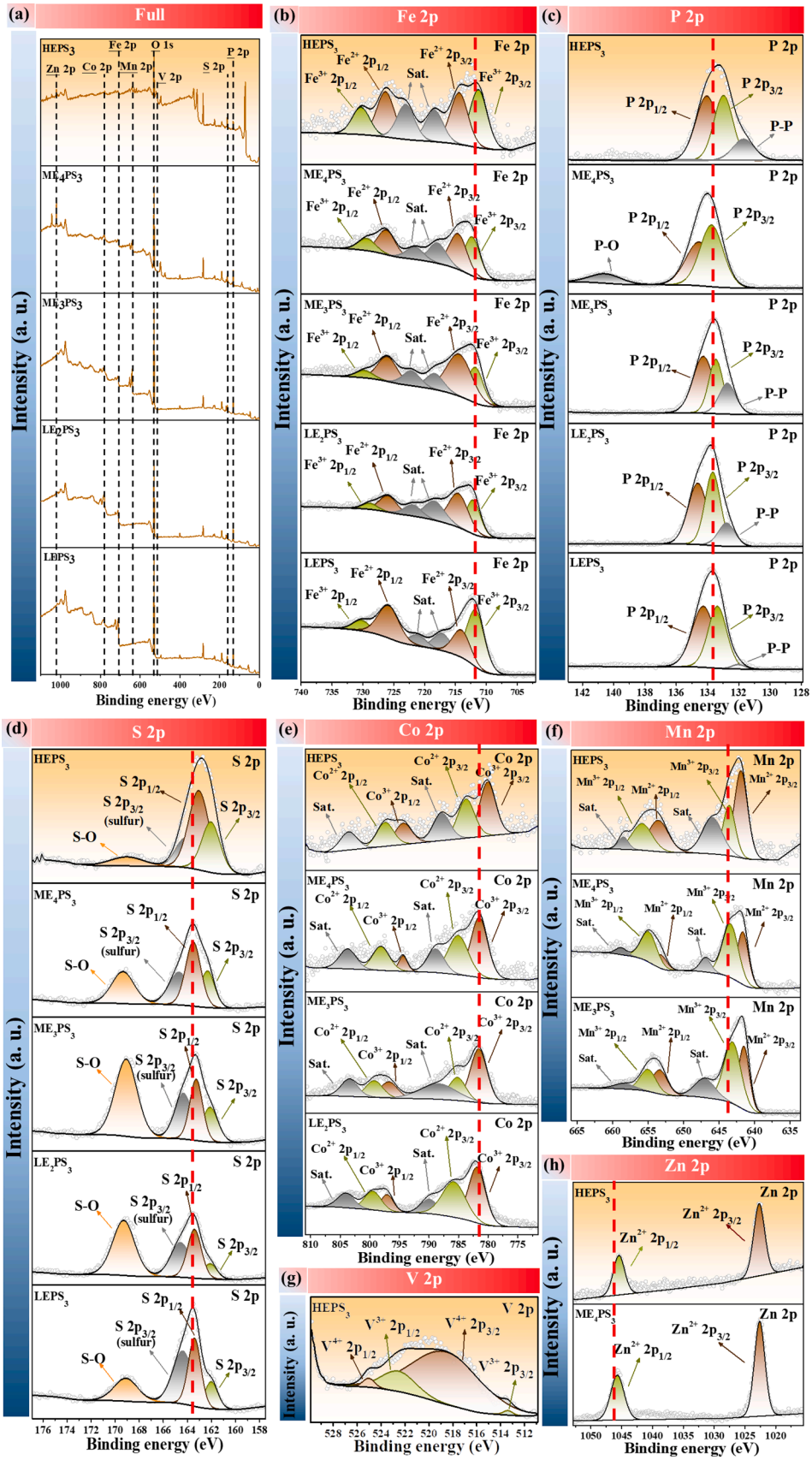

Fig. 3. (a) Full survey XPS spectrum of MPS_3 with different entropy and high-resolution XPS spectrum of (b) Fe 2p, (c) P 2p, (d) S 2p, (e) Co 2p, (f) Mn 2p, (g) V 2p and (h) Zn 2p of MPS_3 with different configurational entropy.

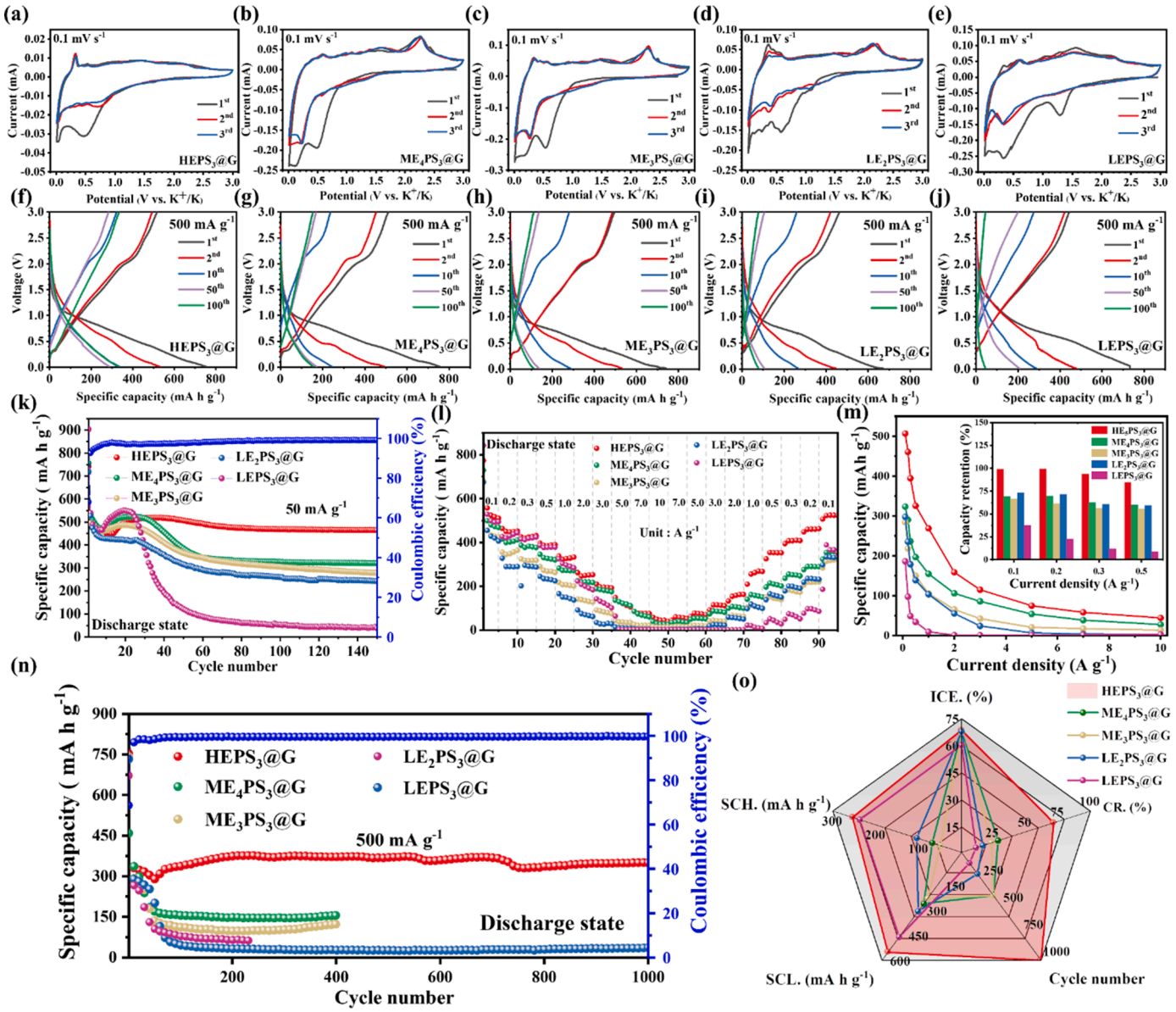

Fig. 4. (a-e) CV curves at 0.1 mV s^{-1} and (f-j) GCD curves of MPS_3@G with different entropy. (k) Cycling performance at 50 mA g^{-1}. (l) Rate capability when the current densities are in the range from 0.1 A g^{-1} to 10 A g^{-1}, and (m) the corresponding specific capacities from 10 A g^{-1} back to 0.1 A g^{-1}. Insets present the capacity retention at various current densities. (n) Long-term cycling performance of $HEPS_3$@G at 500 mA g^{-1}. (o) Comparison results of initial Coulombic efficiency (ICE), cycle retention (CR), low-rate specific capacity at 50 mA g^{-1} (SCL), high-rate specific capacity at 3.0 A g^{-1} (SCH), and cycle number with previous works.

that the thickness is about 7 nm. The scanning electron microscope (SEM) image of the synthesized $HEPS_3$ clearly shows a typical layered stacking morphology with a size of about 10 μm, and corresponding elements (Co, V, Mn, Fe, Zn, P, and S) are evenly distributed in the SEM-EDS mapping (Fig. S3) [32]. The TEM images provide valuable insights into the layered morphology of the $HEPS_3$ nanosheets, which measure approximately 500 nm in lateral size (Fig. 2f). Upon closer inspection via HRTEM (Fig. 2g), the sample exhibits a lattice spacing of 0.304 and 0.294 nm, corresponding to the (−112) and (130) crystal planes of the $HEPS_3$ nanosheets, respectively [33,34]. Moreover, the SAED pattern inset in Fig. 2g indicates an ordered and regular pattern of spots, pointing towards the single-crystal structure of the high-entropy nanosheets with good crystallinity. This observation aligns well with the corresponding PXRD pattern. Finally, the TEM-EDS mapping of Co, V, Mn, Fe, Zn, P, and S elements across the $HEPS_3$ nanosheets (Fig. 2h) shows a homogeneous spatial distribution of these elements, further corroborating the absence of phase segregation. $HEPS_3$ nanosheets were mixed with graphite, namely, $HEPS_3$@G, to improve its conductivity and the detailed microstructureswere also explored by XRD (Fig. S8), SEM (Fig. S11), thermogravimetric analysis (TGA) (Fig. S14), and Raman spectroscopy (Fig. S15), which indicate that carbon is uniformly distributed outside $HEPS_3$.

High-resolution X-ray photoelectron spectroscopy (XPS) tests were conducted on $HEPS_3$ high-entropy nanosheets and corresponding transition metal trichalcogenides $MPCh_3$, including ME_4PS_3, ME_3PS_3, LE_2PS_3, and $LEPS_3$, with different configurational entropy. The spectra of $HEPS_3$ reveal the presence of seven main elements (Fig. 3a), including cobalt (Co 2p), vanadium (V 2p), manganese (Mn 2p), iron (Fe 2p), zinc (Zn 2p), phosphorus (P 2p), and sulfur (S 2p), which is consistent with the mapping results of TEM-EDS and SEM-EDS. In Fig. 3b-d, Fe 2p, P 2p, and S 2p spectra of metal trichalcogenides with different configurational entropy are shown. In the Fe 2p spectrum (Fig. 3b), the Fe $2p_{3/2}$ peak is split into two sub-peaks (714.4 and 711.27 eV), corresponding to Fe^{2+} and Fe^{3+}, respectively. In Fe $2p_{1/2}$, two sub-peaks are observed at

726.32 (Fe^{2+}) and 730.3 eV (Fe^{3+}), while the peaks at 718.42 and 723.05 eV are assigned to satellite peaks [26]. The P 2p XPS spectrum (Fig. 3c) presents $2p_{3/2}$ and $2p_{1/2}$ peaks at 132.98 and 134.05 eV, respectively, corresponding to the P-S bonds in the P_2S_6 unit. Notably, except for ME_4PS_3, other samples show a peak about 131.5 eV attributed to the P-P bond. In contrast to other samples with different configurational entropy, the P 2p XPS spectrum of ME_4PS_3 displays a P-O oxidation peak at about 140 eV, suggesting the slight reaction of the sample with oxygen under ambient conditions [35]. The S 2p XPS spectrum (Fig. 3d) shows that the peak at 169 eV corresponds to the S-O bond, which is attributed to the oxidized -SOx- groups in samples. Meanwhile, the first two peaks at 162.04 and 163.04 eV are respectively related to $2p_{3/2}$ and $2p_{1/2}$ from transition metal trichalcogenides, and the third peak at 164.24 eV belongs to $2p_{3/2}$ of sulfur [36]. Fig. 3e displays two spin-orbit doublets and two shakeup satellites in the Co XPS spectrum, which include the Co^{3+} doublet at 780.07 eV (Co $2p_{3/2}$) and 794.34 eV (Co $2p_{1/2}$) as well as the Co^{2+} doublet at 783.72 eV (Co $2p_{3/2}$) and 797.42 eV (Co $2p_{1/2}$). Similar to the XPS spectra of Fe and Co, Mn also exhibits two satellite peaks (Fig. 3f) at 645.64 and 658.35 eV. Additionally, the Mn $2p_{3/2}$ and Mn $2p_{1/2}$ orbital modes are situated at 640.95 and 652.86 eV, which can be separated into Mn^{2+} (641.53/653.34 eV) and Mn^{3+} (643.21/655.66 eV), respectively. In contrast, Fig. 3g displays the V 2p XPS spectrum of $HEPS_3$ high-entropy nanosheets without a shakeup satellite, in which the peak at 513.66 eV belongs to V $2p_{3/2}$ (V^{3+}) and the peak at 522.49 eV corresponds to V $2p_{1/2}$ (V^{3+}). The neighboring modes at 517.48 eV (V $2p_{3/2}$) and 525.04 eV (V $2p_{1/2}$) are attributed to the presence of V^{4+}. Finally, the Zn XPS spectrum (Fig. 3h) only shows a pair of spin-orbit doublets at 1022.2 ($2p_{3/2}$) and 1045.4 ($2p_{1/2}$) eV, which are attributed to Zn^{2+}. It is worth mentioning that the binding energies of Fe 2p, P 2p, S 2p, Co 2p, and Zn 2p in $HEPS_3$ high-entropy nanosheets all shift to lower energy compared with other metal trichalcogenides with different configurational entropy. However, the binding energy of Mn 2p does not show a significant change. These effects can be understood as an interatomic electron transfer between the materials and relaxation effects caused by the screening of nuclear pores around atoms. In this process, some atoms act as electron acceptors (negative shift) or electron donors (positive shift) to other metal atoms [37].

The electrochemical performance of $HEPS_3$@G and other metal phosphorus trichalcogenides with varying configuration entropy was evaluated. The specific capacity is a direct reflection of the utilization efficiency of the conversion products, such as K_2S and K_4P_3, and is calculated based on the active materials, namely metal phosphorus trichalcogenides and graphite. Fig. S16 depicts the cycling performance of the pure $HEPS_3$ electrode, which lacks carbon coating. On comparing the electrochemical performance of $HEPS_3$@G and the pure $HEPS_3$ electrode, it's apparent that the capacity of the pure $HEPS_3$ electrode surpasses that of the $HEPS_3$@G electrode at lower current densities. This is attributed to the lower capacity of graphite. However, similar capacity contributions are observed from both electrodes at higher current densities, implying an increase in conductivity. Of particular note is the exceptional stability demonstrated by the $HEPS_3$@G electrode. Therefore, we confirm that the addition of graphite enhances the performance of the HEPS3 electrode. Initially, CV curves were displayed for $HEPS_3$@G, ME_4PS_3@G, ME_3PS_3@G, LE_2PS_3@G, and $LEPS_3$@G electrodes to reveal their electrochemical properties. The obtained curves, which were for three cycles, had multiple anodic and cathodic peaks associated with the K^+ adsorption/desorption of metal phosphorus trichalcogenides electrodes with varying configurational entropy, as shown in Fig. 4a-e. In the first cycle for all electrodes with differing configurational entropy, a large cathodic peak was observed at around 0.5 V, which disappeared in subsequent cycles. This peak was attributed to the irreversible conversion reaction of metal phosphorus trichalcogenides with K^+ and the solid electrolyte interface (SEI) formed by the decomposition of KFSI. In subsequent cycles, the curves for the $HEPS_3$@G electrode (Fig. 4a) overlapped significantly at 0.7 V, suggesting that the first conversion reaction occurred at this potential, which may be the conversion of $HEPS_3$@G to some potassium polysulfides. During the depotassiation process, all electrodes with varying configurational entropy display a prominent anodic peak at 0.33 V, and two other anodic peaks around 1.5 V and 2.2 V. The reactions at 0.33 V and 1.5 V represent carbon intercalation and phosphorus conversion reactions [38], respectively, while the 2.2 V peak corresponds to the sulfur conversion reaction. These three reactions are all reversible. Notably, the cathodic and anodic curves of the $HEPS_3$@G electrode (Fig. 4a) from the second cycle exhibit greater overlap than other electrodes, suggesting that the potassiumation/depotassiation reaction of the $HEPS_3$@G electrode has excellent electrochemical reversibility and high stability [39]. Due to the cocktail effect of multiple elements, the $HEPS_3$@G electrode displays broader peaks and shifted reaction potentials compared to others different configurational entropy electrode [40]. Fig. 4f-j presents the GCD curves of various electrodes with different configurational entropy at a current density of 50 mA g^{-1} and a working window of 0.01 - 3.00 V. The initial Coulombic efficiencies (ICE) of the $HEPS_3$@G, ME_4PS_3@G, ME_3PS_3@G, LE_2PS_3@G, and $LEPS_3$@G electrodes are 68.7%, 67.7%, 66.8%, 68.0%, and 60.5%, respectively, such irreversible specific capacity loss is caused by the formation of the SEI layer [41]. Besides, the discussion about the improvement of the ICE was shown in Fig. S17. Fig. S17a and Fig. S17b show the GCD curves using DMC-based electrolyte and DME-based electrolyte respectively. The results show that the introduction of DME-based electrolyte achieves high ICE (73.28%), which is higher than 68.7% of DMC-based electrolyte. Higher ICE indicating a stable and superior SEI with an integral surface has been formed on the $HEPS_3$@G electrodes in DME-based electrolyte, which can more effectively inhibit the continuous electrolyte decomposition and contribute to the utilization of the material in batteries. In contrast, the electrolytes of EC/DEC (1:1) showed lower ICE, 25.97% and 19.71%, respectively (Fig. S17c and Fig. S17d). Since the poor ICE originates from the rough surface and cracked interface of EC/DEC(1:1)-induced SEI, the electrolyte will be continuously consumed to grow fresh SEI, leading to rapid capacity fading [42]. Except for the first cycle, the GCD curves are overlapped in following cycles, consistent with the results of the CV curve. Essentially, the loss of initial Coulombic efficiency is lower with larger configurational entropy, which is related to material agglomeration, with materials having lower configurational entropy (such as $LEPS_3$@G) experiencing more severe agglomeration, further reducing electrical activity. It is hypothesized that some potassiated parts of $LEPS_3$@G may not be depotassiated successfully, meaning some K^+ ions are irreversibly trapped, resulting in a lower initial Coulombic efficiency compared to other electrode materials, align with the simulated data. The cycling performance of $HEPS_3$@G at a low current density of 50 mA g^{-1} demonstrates a high reversible capacity of about 500 mAh g^{-1} and a capacity retention of 94.1% after 150 cycles (Fig. 4k). In contrast, the capacities of ME_4PS_3@G, ME_3PS_3@G, and LE_2PS_3@G electrodes begin to decline slowly after 30 cycles and then stabilize at 345 mAh g^{-1}, 338 mAh g^{-1}, and 283 mAh g^{-1} after 60 cycles, respectively. The $LEPS_3$@G electrode has an initial high capacity of 550 mAh g^{-1}, but its capacity drops sharply after 30 cycles. After the 45th cycle, the decreasing trend slows down, and the capacity stabilizes at around 50 mAh g^{-1}. Interestingly, all samples exhibit an initial drop in capacity followed by an increase. This is because the $HEPS_3$@G electrode contains unmodified graphite, which typically shows poor K^+ storage behavior. As a result, during the initial cycling process, the capacity contribution of the graphite gradually diminishes, leading to a decreased initial capacity. In subsequent cycles, the capacity shows an upward trend, attributable to the activation of phosphorus and the optimization of the solid electrolyte interphase (SEI) layer. Given phosphorus's poor conductivity and the insignificant enhancement in conductivity provided by the alloy layer, a larger number of cycling cycles is required to fully activate the phosphorus. Additionally, the capacity increase is partly due to the optimization of the SEI layer, facilitated by electrochemical reconstruction. To

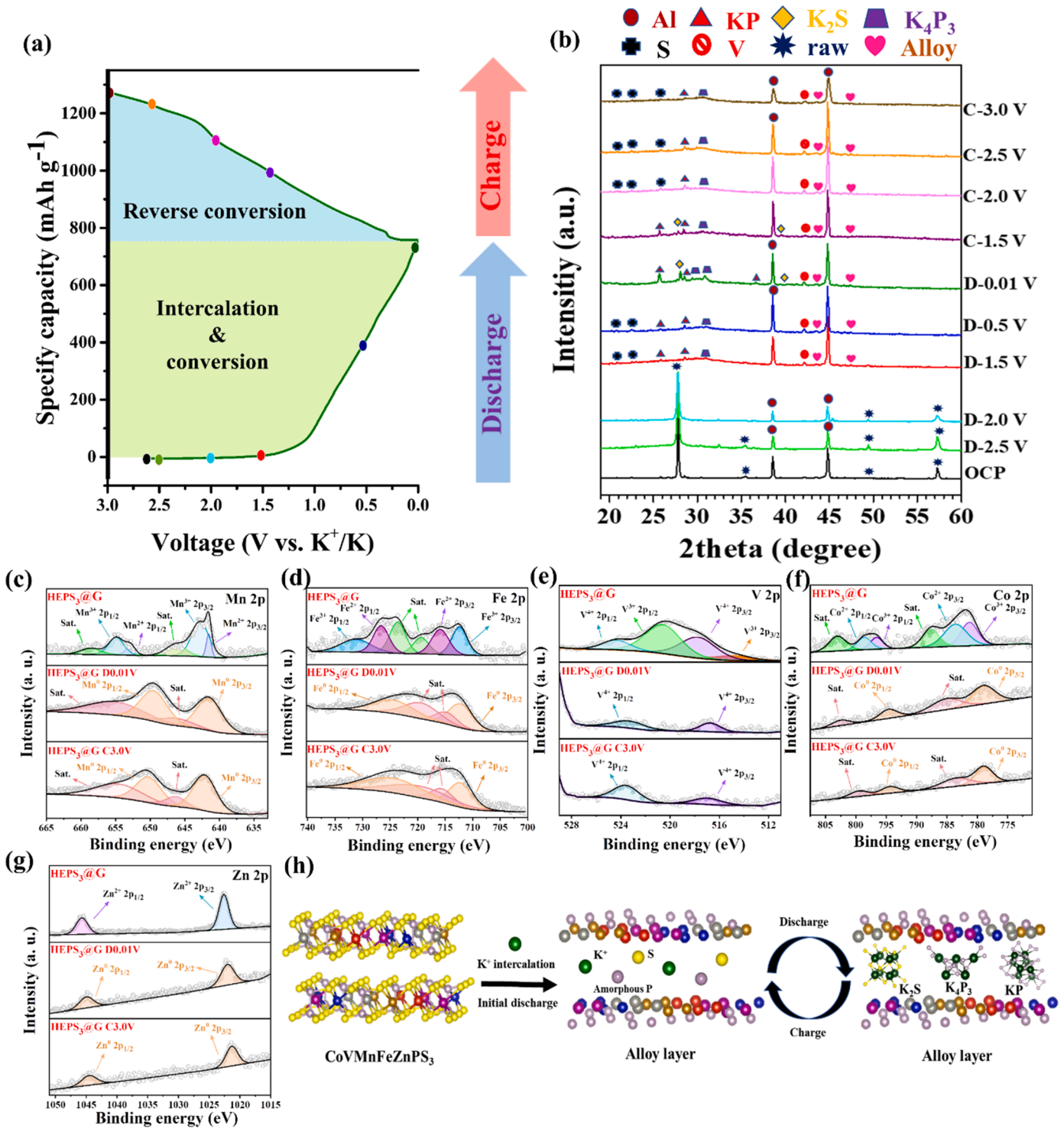

Fig. 5. (a) First cycle charge/discharge profile of $HEPS_3$ (using the KFSI electrolyte) tested at 50 mA g^{-1} with selected potentials for the ex situ XRD analyses presented in (b). (c) Ex situ XPS analysis of $HEPS_3$@G electrodes before/after cycling. Comparison of the (c) Co 2p, (d) Mn 2p, (e) Fe 2p, (f) V 2p and (g) Zn 2p core-level spectra for the material in the pristine, fully potassiated (discharged to 0.01 V) and depotassiated (charged to 3.0 V) states. (h) Schematic illustration of the K^+ storage mechanism of the $HEPS_3$ electrode during charging/discharging process.

further evaluate the beneficial impact of the high-entropy effect on the electrochemical performance during charge/discharge, the rate performance of different kinds of entropy materials was investigated. All anode materials were tested under a condition of continuously varying current density, ranging from 0.1 A g^{-1} to 10 A g^{-1} (Fig. 4I). From the rate performance results, it can be observed that as the current density increases, the performance gap between $HEPS_3$ and the different entropy samples continues to narrow. There is no significant difference observed at current densities higher than 5 A g^{-1}. This phenomenon can be attributed to the low conductivity contribution of alloy layer, rendering it indistinguishable from other samples at high rate performance. The composition of multiple elements induces a lattice distortion effect, which in turn increases the scattering of propagating electrons and phonons. This is not favorable for enhancing electrical conductivity,

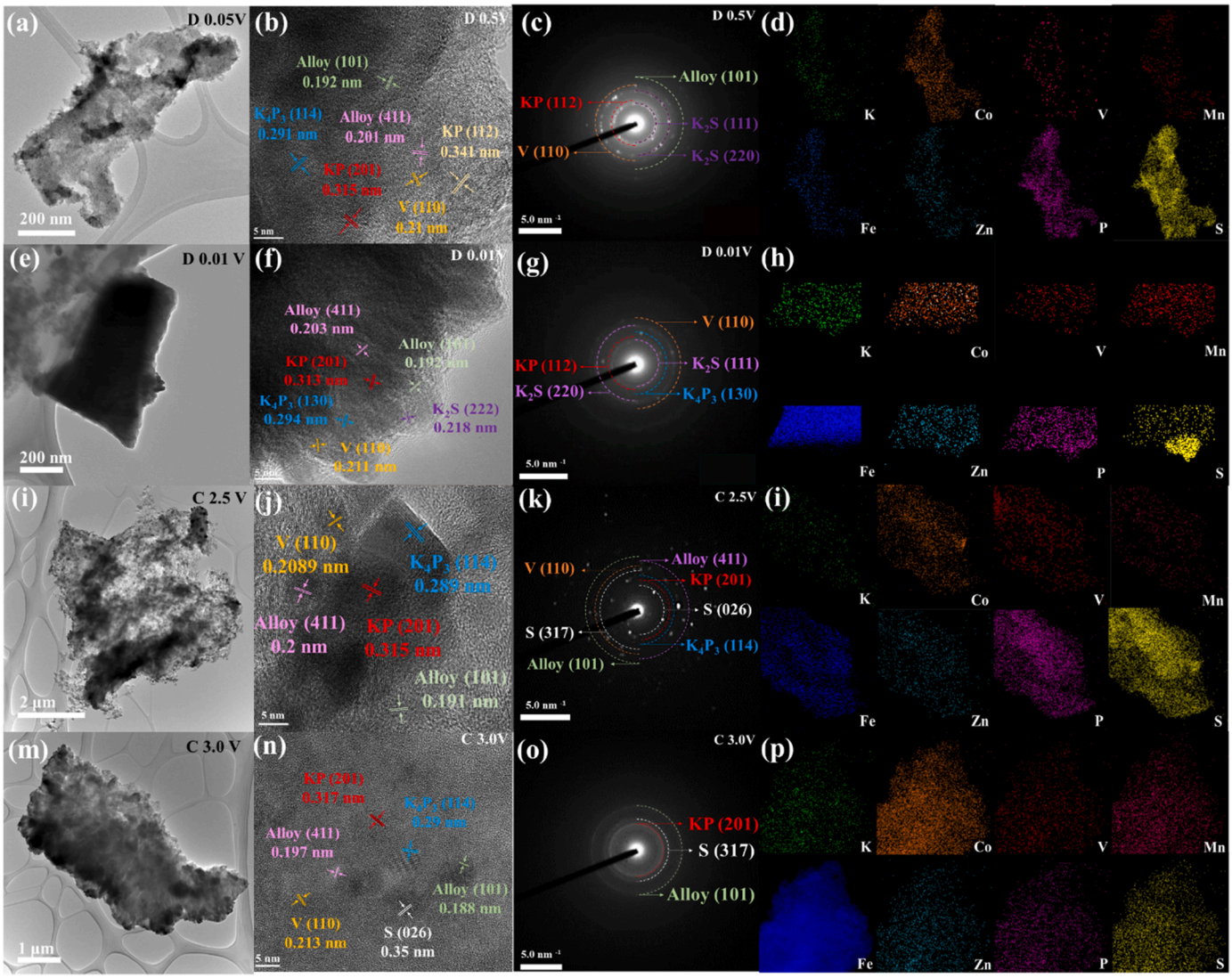

Fig. 6. Low magnification TEM images, HRTEM images, SAED patterns and EDS elements mapping of the cycled $HEPS_3$: (a-d) discharged to 0.5 V (e-h) discharged to 0.01 V (i-l) charged to 2.5 V (m-p) charged to 3.0 V.

resulting in no conspicuous difference in high-rate performance. However, the lattice distortion effect improves the mechanical strength of the material. After exposure to high current densities, when the system returns to a lower current density, the $HEPS_3$ electrode can effectively recover to its capacity prior to the high-current exposure, demonstrating good mechanical strength. Therefore, the absence of a significant advantage at high rate performance is primarily because the alloy layer contributes more to improving mechanical strength than it does to enhancing conductivity.

Fig. 4m summarizes the specific capacities of electrodes with different configurational entropy from 10 A g^{-1} back to 0.1 A g^{-1}. Basically, as the configuration entropy increases, the specific capacity of the electrode is higher. At lower current densities, the specific capacity gap between high-entropy electrodes and other electrodes is particularly pronounced. Compared with ME_4PS_3@G, ME_3PS_3@G, and LE_2PS_3@G, $HEPS_3$@G has a higher reversible capacity of about 100 mAh g^{-1} at a current density of 1 A g^{-1}. When the electrode returns to the current density of 0.1 A g^{-1}, the gap of specific capacity is higher than 200 mAh g^{-1}, comparing with $LEPS_3$@G is even higher than 300 mAh g^{-1}. The inserted column graph in Fig. 4m shows the relationship between the capacity retention of different entropy electrodes and various current densities. At a current density of 0.1 A g^{-1}, the capacity retention of $HEPS_3$@G, ME_4PS_3@G, ME_3PS_3@G, LE_2PS_3@G and $LEPS_3$@G were 99.2%, 69.1%, 66.9%, 73.2% and 37.6%, respectively. It can be seen that $HEPS_3$@G has better capacity retention than other materials with different configuration entropy, while the capacity retention of ME_4PS_3@G, ME_3PS_3@G and LE_2PS_3@G is about the same level, and finally $LEPS_3$@G has the worst capacity retention. The similar situation is also observed at lower rate current densities (such as 0.2, 0.3, and 0.5 A g^{-1}), demonstrating the advantage of the high-entropy configuration.

The $HEPS_3$@G electrode demonstrates higher specific capacities at different current densities and shows remarkable long-term cycling stability even at a high rate of 500 mA g^{-1} (Fig. 4n). After 1000 cycles, the $HEPS_3$@G electrode still provides a reversible capacity of about 340 mA h g^{-1} and an average Coulombic efficiency of 99.95%. This high Coulombic efficiency is attributed to the surface treatment of the structure and uniform contact with the electrolyte. The excellent cycling performance and rate capability of $HEPS_3$@G are supported in these results. Finally, metal phosphorus trichalcogenides anodes with various configurational entropy were compared in the radar diagram of Fig. 4g [43], considering five aspects: initial Coulombic efficiency (ICE), low-rate specific capacity at 50 mA g^{-1} (SCL), high-rate specific capacity at 500 mA g^{-1} (SCH), cycle number, and capacity retention (CR). The irreversible reactions in the initial cycle led to initial Coulombic efficiencies of less than 70% for all materials due to the inevitable capacity loss of the conversion reaction. The $HEPS_3$@G electrode not only

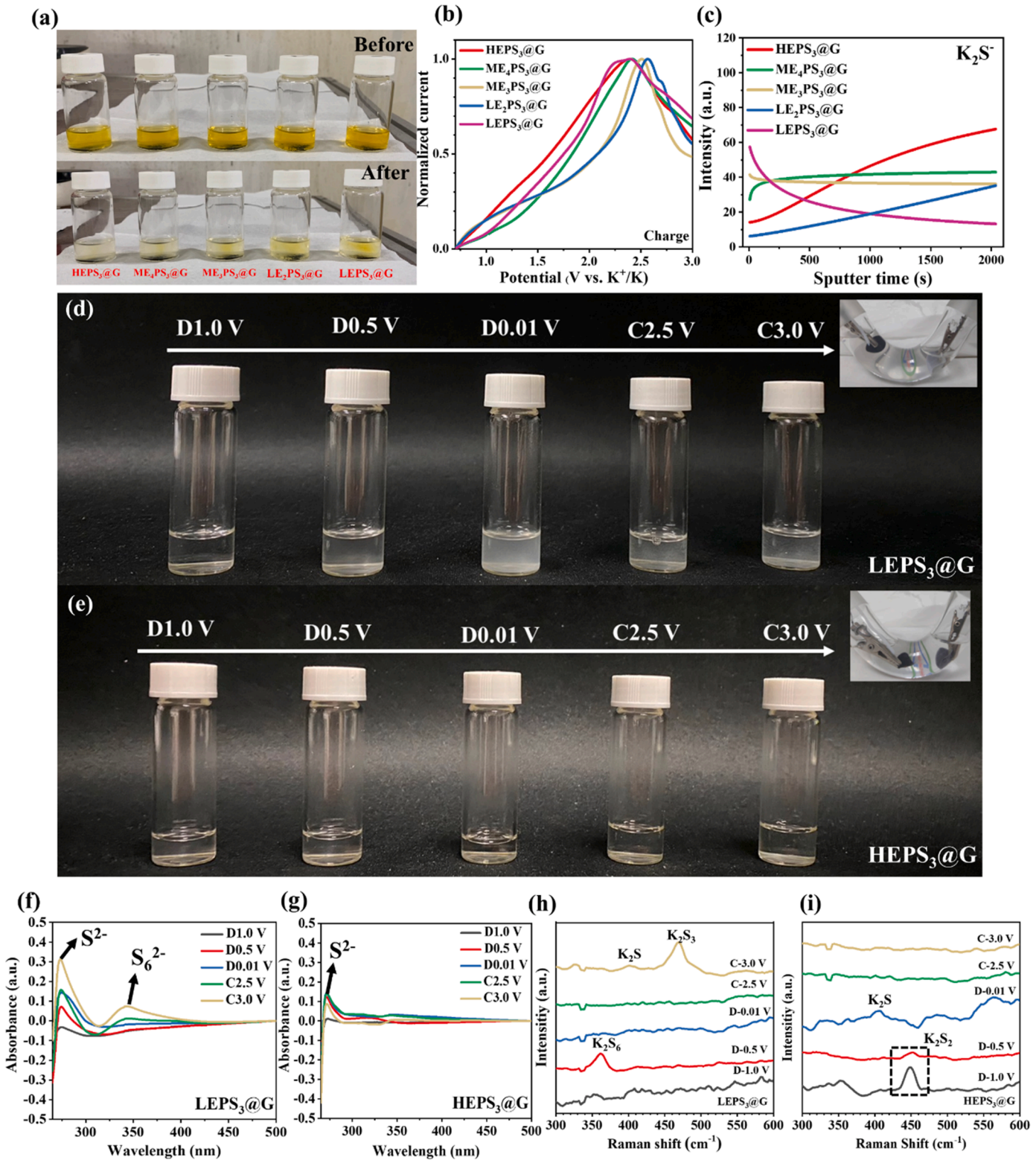

Fig. 7. Potassium polysulfides adsorption experiment. (a) Chemical adsorption method performed by $HEPS_3$@G, ME_4PS_3@G, ME_3PS_3@G, LE_2PS_3@G and $LEPS_3$@G. (b) LSV profiles with a scan rate of 5.0 mV s^{-1}. (c) Negative-mode ToF-SIMS depth profiles of K_2S^- in fully charged after 20 cycles. "Transparent" batteries the dissolution and shuttling behavior of the polysulfide intermediates in (d) $LEPS_3$@G electrode and (e) $HEPS_3$@G electrode. Raman spectra of (f) $LEPS_3$@G anode and (g) $HEPS_3$@G anode at various discharge/charge stages corresponded in panel (d,e). UV–Vis spectrum of (h) $LEPS_3$@G anode and (i) $HEPS_3$@G anode at various discharge/charge stages corresponded in panel (d,e).

exhibits significant specific capacity at both low and high current rates but also achieves a cycle capability of up to 1000 cycles, thanks to the unique lattice distortion effect of high-entropy materials.

To elucidate the impact of structural evolution and the relatively high-entropy configuration at the interface, we conducted a comprehensive investigation into the electrochemical mechanism of K^+ storage in the $HEPS_3$ electrode during the initial discharge/charge process. This was accomplished through ex situ X-ray diffraction (XRD) and ex situ X-ray photoelectron spectroscopy (XPS) analyses [44]. Ex situ XRD analysis was employed to measure the discharge/charge of the battery within a voltage range of 0.01 V to 3.00 V, as depicted in Fig. 5a and 5b. At the initial open circuit voltage (OCV, approximately 2.7 V vs K^+/K), the diffraction peaks corresponding to the (002), (131), (202), and (060) planes were clearly observed at 27.8°, 35.5°, 49.4°, and 57.2°, respectively. No significant peak changes were detected when the cell was discharged to 2.5 V and 2.0 V, suggesting that K^+ ions intercalate into the material, forming K_xHEPS_3. As the cell discharged further, the diffraction peaks of K_xHEPS_3 gradually vanished, and new peaks emerged at 20.8°, 22.5°, 25.8°, 28.6°, 30.9°, 42.1°, 43.6°, and 47.4° Specifically, the peaks at 20.8° and 22.5° were associated with the generation of sulfur, while those at 25.8° and 28.6° corresponded to the formation of KP. The peaks at 30.9° and 42.1° represented the K_4P_3 and metallic vanadium (V) phases, respectively. Lastly, the peaks at 43.6° and 47.4° indicated the reduction of high-entropy alloys from $HEPS_3$ during the potassiation process. When the cell discharged to 0.5 V, the diffraction peak attributed to sulfur weakened, and a new peak for K_2S appeared at 28.1°, signifying the occurrence of a sulfur conversion reaction [45]. As the cell continued to discharge to 0.01 V, the K_2S, KP, and K_4P_3 phases intensified, indicating that the conversion reaction had fully completed. During the subsequent charging process, the diffraction peaks for K_2S and KP gradually disappeared, and the signal intensities of KP and K_4P_3 diminished. However, the diffraction peaks of KP and K_4P_3 are still exist. As a result, KP and K_4P_3 partially converse to amorphous P during the charging process. Conversely, the diffraction peaks of sulfur re-emerged. Therefore, the $HEPS_3$ electrode's reaction mechanism during the potassiation/depotassiation processes can be described as follows:

Discharge

Stage I: $CoVMnFeZnPS_3 + K^+ + e^- \rightarrow K_xCoVMnFeZnPS_3$ (OCP to 2.0 V)

Stage II: $CoVMnFeZnPS_3 + K^+ + e^- \rightarrow V + (CoMnFeZn)alloy + K_4P_3 + KP + S$ (~1.5 V)

Stage III: $S + K^+ + e^- \rightarrow K_2S$ (~ 0.01 V)

Charge

Stage IV: $K_4P_3 + KP \rightarrow Amorphous\ P + K_4P_3 + KP + K^+ + e^-$ (limited reactivity during depotassiation process)

Stage V: $K_2S \rightarrow S + K^+ + e^-$ (~2.0 V)

Subsequent cycle

Stage VI: $Amorphous\ P + S + K^+ + e^- \leftrightarrow KP + K_4P_3 + K_2S$

Furthermore, ex situ XPS analysis was performed after the first discharge and charge (Fig. 5c–g) to better understand the role of each metal component in $HEPS_3$. As expected, the cation valences were $Co^{2+/3+}$, $Fe^{2+/3+}$, $Mn^{2+/3+}$, $V^{3+/4+}$ and Zn^{2+} for the initial state samples, respectively. Once discharged to 0.01 V, the Co 2p, Fe 2p, and Mn 2p spectra showed reduction of $Co^{2+/3+}$ to Co^0 (780.94 and 793.4 eV), $Fe^{2+/3+}$ to Fe^0 (712.19 and 724.41 eV), $Mn^{2+/3+}$ to Mn^0 (641.46 and 649.47 eV) and Zn^{2+} to Zn^0 (1044.9 and 1021.9 eV) [46], indicating that all multivalent cations in the $HEPS_3$ lattice were reduced to M^0. When the cell charged to 3.0 V, the binding energy of all transition metals were the same as discharging to 0.01 V, indicating that the irreversible structural transformation of transition metals occurred after the initial discharge process, and all transition metals were remained in the M^0 state. It's worth mentioning that although the V spectra does not have the trend of a M^0 peak as other transition metals during the charge/discharge process, the metal V always exists after discharging to 1.5 V in the first cycle by observing the ex situ XRD patterns (Fig. 5b). Finally, we demonstrate the crystal structures of the corresponding phases change during charge/discharge process as shown in Fig. 5h. We refer that $HEPS_3$ generates a sheet-like architecture made up of transition metal alloys, metallic vanadium, and amorphous phosphorus following the initial discharge. Simultaneously, K^+, S, and sections of the amorphous phosphorus partake in a reversible conversion reaction occurring amidst the sheets. Notably, the verification of the sheet-like morphology and its composition will lately be confirmed by observing the ex situ TEM images and HRTEM images respectively at different potentials in Fig. 6.

We investigated the morphology and crystallography of the cycled $HEPS_3$ anode using ex situ TEM and HRTEM. Fig. 6a, 6e, 6i, and 6m display TEM images of the $HEPS_3$ electrode at various stages of discharging and charging (0.5 V, 0.01 V, 2.5 V, and 3.0 V, respectively), revealing a consistent sheet-like morphology throughout the cycling process. Ex situ HRTEM and SAED analysis were conducted to examine the $HEPS_3$ electrode at different charge and discharge states during the first cycle. For the cell discharged to 0.5 V, the HRTEM image in Fig. 6b clearly shows several calculated lattice spacings of 0.192, 0.201, 0.21, 0.291, 0.341, and 0.315 nm. The lattice spacings of 0.192 and 0.201 nm correspond to the (101) and (411) crystal planes of the alloy, while the spacings of 0.21 and 0.291 nm can be indexed as (110) and (114) crystal planes of metallic vanadium and K_4P_3, respectively. Lastly, the lattice spacings of 0.341 and 0.315 nm represent the (112) and (201) crystal planes of KP. The SAED pattern in Fig. 6c, discharged to 0.5 V, aligns with ex situ XRD and XPS results and includes the (101) crystal plane of the alloy, the (110) crystal plane of metallic vanadium, the (112) crystal plane of KP, and the (111) and (220) crystal planes of K_2S. Furthermore, the EDS mapping in Fig. 6d demonstrates a uniform elemental distribution, which supports the formation of high-entropy alloys and K^+ intercalation. When the battery is discharged to 0.01 V, the HRTEM image (Fig. 6f) exhibits the same lattice spacings as the one discharged to 0.5 V. However, an additional lattice spacing of 0.218 nm, corresponding to the (222) crystal plane of K_2S, is observed. Additionally, the (130) crystal plane of K_4P_3 is evident in the SAED pattern at 0.01 V discharge (Fig. 6g). The EDS mapping results in Fig. 6h reveal stronger intensity for K^+ and other transition metals, indicating the completion of K^+ reactions and the formation of high-entropy alloys, which exhibit sheet-like morphology and even elemental distribution. During the charging process, the poor reversibility of P results in the presence of 0.315 nm and 0.29 nm lattice spacings, formed by the (201) crystal plane of KP and (114) crystal plane of K_4P_3, in the HRTEM images (Fig. 6j, n). The (110) crystal plane of metallic vanadium and the (411) and (101) crystal planes of the high-entropy alloy remain a stable state during cycling processes, as confirmed by ex situ XRD. This indicates the formation of an irreversible high-entropy alloy layered structure due to the effective (de)intercalation of K^+ ions into the host structure during the charge/discharge process. The SAED patterns at two charging potentials (Fig. 6k, o) further reveal the formation of high-entropy alloys through irreversible reactions and the creation of S via reversible conversion reactions. The ring patterns in Fig. 6k and 6o indicates metallic V, Alloy, and elemental S corresponded to crystal planes of (110), (101)/(411), and (317)/(026) which are in line with the findings from the ex situ analysis. Lastly, Fig. 6i and 6p display the EDS mapping results for the battery charged to 2.5 V and 3.0 V, respectively, revealing the presence of distinct elements without any apparent phase separation.

Fig. 7a illustrates the effect of $HEPS_3$@G, ME_4PS_3@G, ME_3PS_3@G, LE_2PS_3@G, and $LEPS_3$@G composites on potassium polysulfides [47]. In the experiment, 30 mg of K_2S was added to 5 ml of DMC solution to create a saturated solution. Once fully dispersed, 5 ml of the clear upper liquid was extracted using a needle, and then 5 mg of five distinct high-entropy metal phosphorus trichalcogenides compounds were added separately. After 20 min in suspension, the five solutions gradually transitioned from light yellow to transparent, with the $HEPS_3$@G compound solution being the closest to complete transparency. As the configurational entropy decreases, the color of solution becomes more yellow, indicating a reduced ability of the compounds to capture K_2S

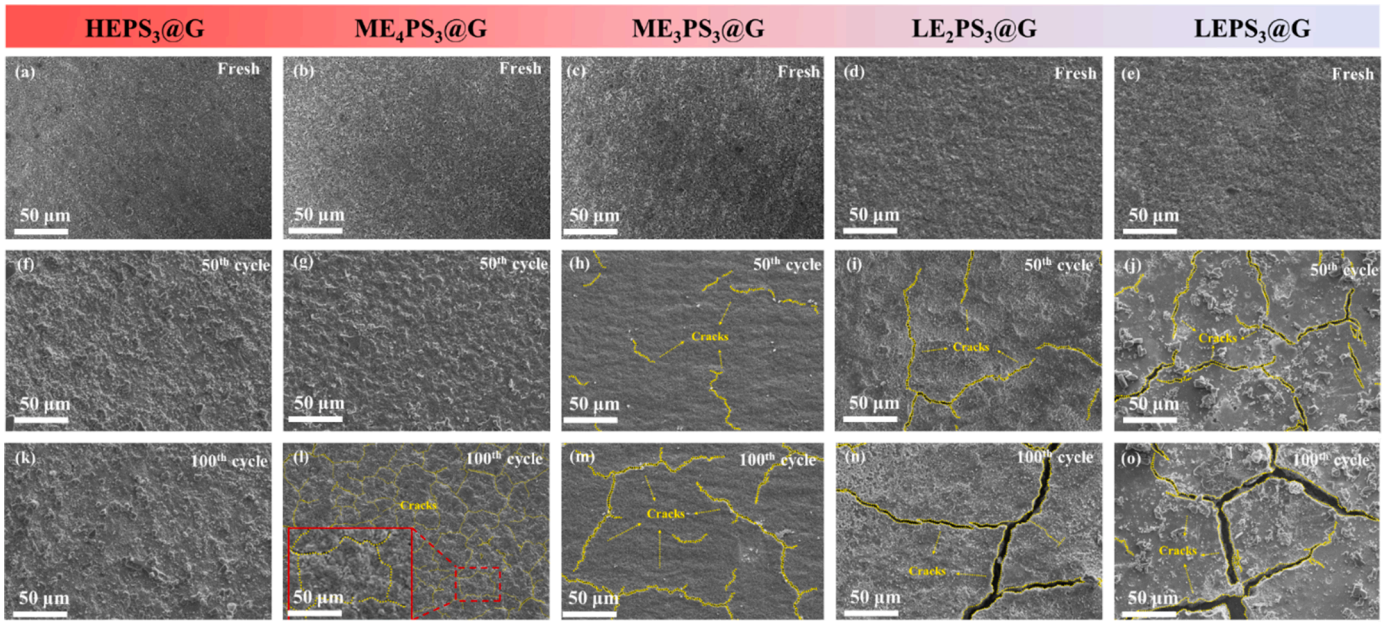

Fig. 8. SEM images of electrode surface. (a-e) Top view of $HEPS_3$@G, ME_4PS_3@G, ME_3PS_3@G, LE_2PS_3@G and $LEPS_3$@G electrodes (a-e) before cycling and after cycling: (f-j) 50^{th} cycle (k-o) 100^{th} cycle.

and a higher concentration of K_2S remaining in the solution. Consequently, the solution containing $LEPS_3$@G exhibits the most intense yellow color, indicating its inferior ability to capture K_2S. Conversely, the color of solution becomes more transparent with increasing configurational entropy, implying an enhanced ability to capture K_2S. Additionally, we conducted LSV to examine the sulfur oxidation behavior of various compound materials, as shown in Fig. 7b. An anodic peak associated with the oxidation of K_2S to elemental S is observed. Compared to the ME_4PS_3@G, ME_3PS_3@G, and LE_2PS_3@G electrodes, the HEPS3@G and $LEPS_3$@G electrodes display smaller polarization and higher redox peaks, suggesting improved redox kinetics. Moreover, considering the larger oxidation peak area and lower peak potential, the $HEPS_3$@G and $LEPS_3$@G electrodes actively catalyze the conversion of K_2S to elemental S. Notably, the ME_4PS_3@G electrode exhibits a lower peak potential than the ME_3PS_3@G and LE_2PS_3@G electrodes [48]. Therefore, the catalytic activity for the oxidation of K_2S can be expressed in the order of $HEPS_3@G = LEPS_3@G > ME_4PS_3@G > ME_3PS_3@G >$ LE_2PS_3@G [49].

Moreover, we carried out time-of-flight secondary ion mass spectrometry (TOF-SIMS) tests on the electrode surfaces of $HEPS_3$@G, ME_4PS_3@G, ME_3PS_3@G, LE_2PS_3@G, and $LEPS_3$@G after 20 cycles (Fig. 7c). The results reveal distinct differences among these five electrode materials. As the configurational entropy of material increases, the concentration of K_2S at 2000 s is higher, indicating more K_2S is trapped within the material. Consequently, the $HEPS_3$@G electrode exhibits the strongest ability to capture K_2S. Additionally, the concentration of K_2S on the $LEPS_3$@G electrode surface is initially the highest but decrease after 700 s, suggesting that K_2S dissolves into the electrolyte during cycling. These findings are consistent with the chemical adsorption experiments in Fig. 7a. To visualize the effect of high-entropy materials on K_2S, we fabricated "transparent" cells (Fig. 7d, e). In this experiment, we extracted 1 ml of electrolyte from each potential (0.1 V, 0.5 V, and 0.01 V during discharge and 2.5 V and 3.0 V during charge) into a small sample bottle to observe the color change [50]. We found that when the $LEPS_3$@G electrode was discharged to 0.5 V, the electrolyte began to exhibit slight white turbidity, attributed to the formation of K_2S and its subsequent dissolution into the solution. As further discharging to 0.01 V, electrolyte become to more evident white turbidity, indicating the complete conversion of sulfur in the material into K_2S. While charging the electrode to 2.5 V and 3.0 V, the white-and-turbid electrolyte implies poor reversibility of K_2S. In contrast, the $HEPS_3$@G electrode displayed transparent and clear electrolyte at different potentials, indicating no significant polysulfide shuttle effect and a strong ability to capture K_2S. This result is consistent with the previous experimental findings and the long-term cycling performance of the battery. Subsequently, we performed ultraviolet-visible (UV–Vis) tests on the electrolyte extracted from the "transparent" battery at different potentials (Fig. 7f, g). The electrolyte of the $LEPS_3$@G electrode exhibited two peaks at 274 nm and 343 nm, corresponding to S^{2-} and S_6^{2-}, respectively. During the charge/discharge process, the concentration of both sulfide ions increased, indicating an intensifying shuttle effect. In contrast, the electrolytes of the $HEPS_3$@G electrode displayed only the peak of S^{2-}. The concentration of S^{2-} is peaked when the battery was discharged to 0.01 V, then decreased with charging, indicating no significant polysulfide shuttle effect [51]. Raman spectra of the $LEPS_3$@G and $HEPS_3$@G electrodes at different potentials are shown in Fig. 7h and 7i, respectively. For the $LEPS_3$@G electrode, the appearance of K_2S_6, K_2S, and K_2S_3 peaks during discharge and charge indicated the presence of potassium polysulfides existed in electrolyte and surface of electrode surface due to irreversible reactions [52]. In contrast, the $HEPS_3$@G electrode displayed peaks corresponding to K_2S_2 and K_2S during discharge, but no potassium polysulfide peaks at fully charge state. This observation indicates the absence of dissolved potassium polysulfides in the electrolyte and their absence on the electrode surface during charge (Fig. 7i), showing that the $HEPS_3$@G electrode demonstrates effective catalytic activity for K_2S [53,54]. The low overpotential and robust capture ability for K_2S not only suppress the shuttle effect but also promote polysulfides reversibility in electrochemical reactions.

The mechanical stability of transition metal phosphorus trichalcogenide electrodes with varying configurational entropies were examined by the SEM images of each electrode under different cycle numbers [55]. Pristine electrodes of $HEPS_3$@G, ME_4PS_3@G, ME_3PS_3@G, LE_2PS_3@G, and $LEPS_3$@G (Fig. 8a-e) revealed smooth surfaces devoid of fine cracks or voids [56], as they had not yet undergone K^+ insertion or extraction, and thus, no volume changes occurred [57]. We cycled these five electrodes 50 times at 1C (500 mA g^{-1}) (Fig. 8f-j). The surfaces of $HEPS_3$@G and ME_4PS_3@G remained smooth and flat, similar to their pre-cycle states. However, noticeable cracks emerged on the lower

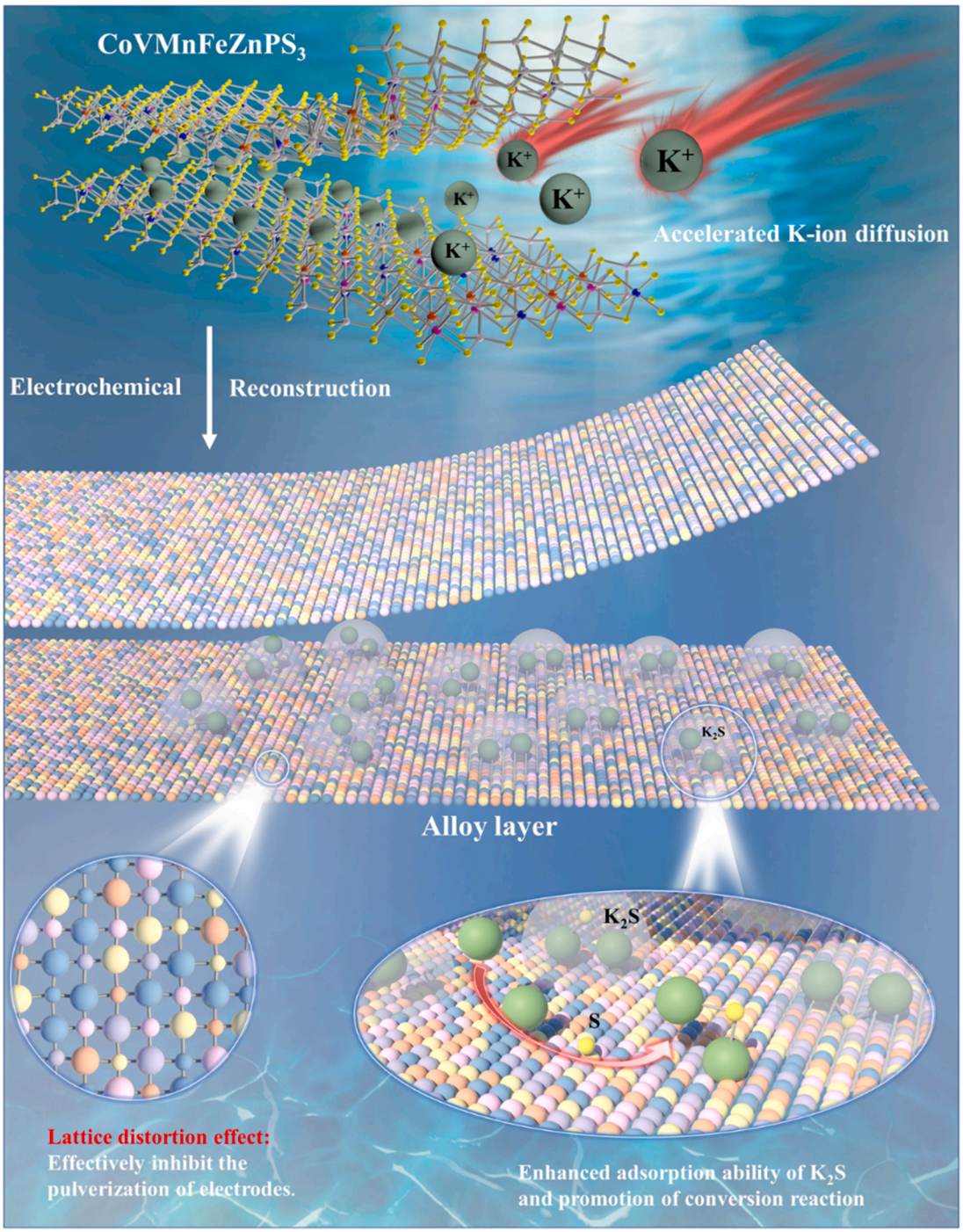

Fig. 9. Schematic diagram of the electrochemical reconstruction process and dual properties of the $HEPS_3$ nanosheet electrode, which are beneficial for producing the non-cracked electrode due to lattice distortion effect and can inhibit the shuttle effect.

configurational entropy materials ME_3PS_3@G, LE_2PS_3@G, and $LEPS_3$@G, with fragmentation severity increasing as configurational entropy decreased [58]. These cracks primarily resulted from anisotropic volume changes in randomly oriented primary gains, leading to extended K^+ diffusion paths, non-uniform K^+ concentrations within the electrode material, additional stress, and ultimately, surface cracking [59]. Higher configurational entropy materials ($HEPS_3$@G and ME_4PS_3@G) exhibited greater compositional disorder, promoting elemental mixing and stable solid solution phases, as opposed to more brittle materials. The inclusion of atoms of varying sizes in $HEPS_3$@G caused lattice distortion, which enhanced properties such as hardness and strength, mitigating volume changes during charge and discharge processes. After 100 cycles (Fig. 8k-o), the $HEPS_3$@G electrode surface remained smooth, while the ME_4PS_3@G surface displayed shallow micro-scratches. The ME_3PS_3@G electrode exhibited increased surface cracking compared to its 50-cycle state [60]. Severe and deep internal cracks were observed on LE_2PS_3@G and $LEPS_3$@G surfaces (Fig. 8n, o), attributable to substantial, non-uniform internal stress generated during cycling. In summary, increased configurational entropy corresponded to reduced surface fragmentation, with the $HEPS_3$@G electrode demonstrating the strongest ability to resist electrode stress changes and alleviate internal stress due to its highest configurational entropy. These results align with long-term electrochemical performance, further validating the superior cycle stability of the $HEPS_3$@G electrode compared

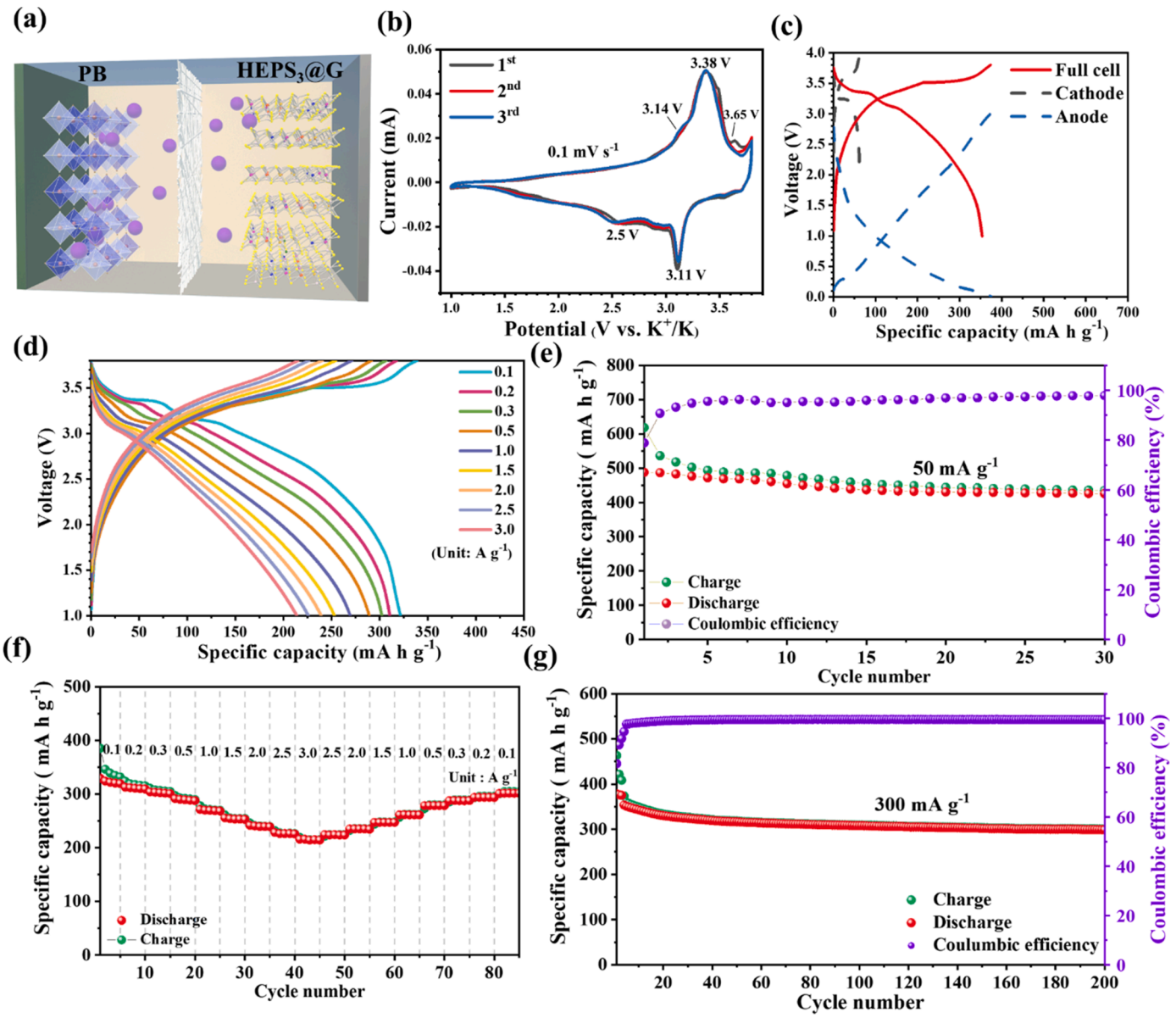

Fig. 10. Full cell of $HEPS_3$@G//PB. (a) Schematic diagram of a $HEPS_3$@G//PB full cell. (b) CV curves of the full cell at 1st~3th cycle. (c) GCD curves of the PB half cell, $HEPS_3$@G half cell and $HEPS_3$@G //PB full cell. (d) GCD curves and (e) Cycling performance at 50 mA g^{-1}. (f) Rate capability when the current densities are in the range from 0.1 to 3.0 A g^{-1}. (g) Long-term cycling performance at 300 mA g^{-1} of the $HEPS_3$@G//PB full cell.

to other materials.

Our findings reveal that the $HEPS_3$@G anode exhibits a dual effect on PIBs by simultaneously inhibiting the polysulfide shuttle effect and alleviating mechanical stress accumulated by K^+ during repeated insertion/extraction processes (Fig. 9). After the initial reaction, $HEPS_3$ forms an alloy layer composed of four elements, and this alloy layer is influenced by lattice distortion, resulting in increased scattering of electron and phonon propagation. While this may enhance the material's mechanical strength, it hinders electrode conductivity. Additionally, the potassiation process gradually progresses from the exterior to the interior of the material, indicating that the alloy layer will first form on the outer surface, impeding the electrochemical reconstruction within the material. Therefore, having excellent K^+ diffusion performance from the beginning is beneficial for the complete progress of the electrochemical reconstruction reaction. Since this reaction is irreversible and does not revert to the $HEPS_3$ phase, our initial simulations are not applicable for subsequent cycles. Thus, GITT curves of the $HEPS_3$ electrode at first and second cycle were provided (Fig. S34). There is no significant difference in the average diffusion coefficient of potassiation process between the first and the second cycle, indicating that the alloy layer has no obvious influence on the ability of K^+ transfer. This structure has been experimentally demonstrated, through chemical adsorption experiments, SIMS, LSV, and "visualization" batteries, to effectively capture polysulfides and catalyze their conversion, accelerating electron transport and contributing to the high reversible capacity observed in electrochemical performance. Moreover, the sheet-like alloy material, formed via electrochemical restructuring, exhibits a unique "lattice distortion effect" due to its high configurational entropy, which enhances the mechanical stability and structural stability of the material. Consequently, the electrode is less prone to cracking during potassiation/depotassiation processes, consistent with our observation of an uncracked $HEPS_3$@G electrode surface after potassiation/depotassiation. Therefore, the $HEPS_3$@G electrode represents a promising advancement in electrode material design by combining the high-entropy material cocktail effect with the tunable interlayer spacing of 2D nanomaterials.

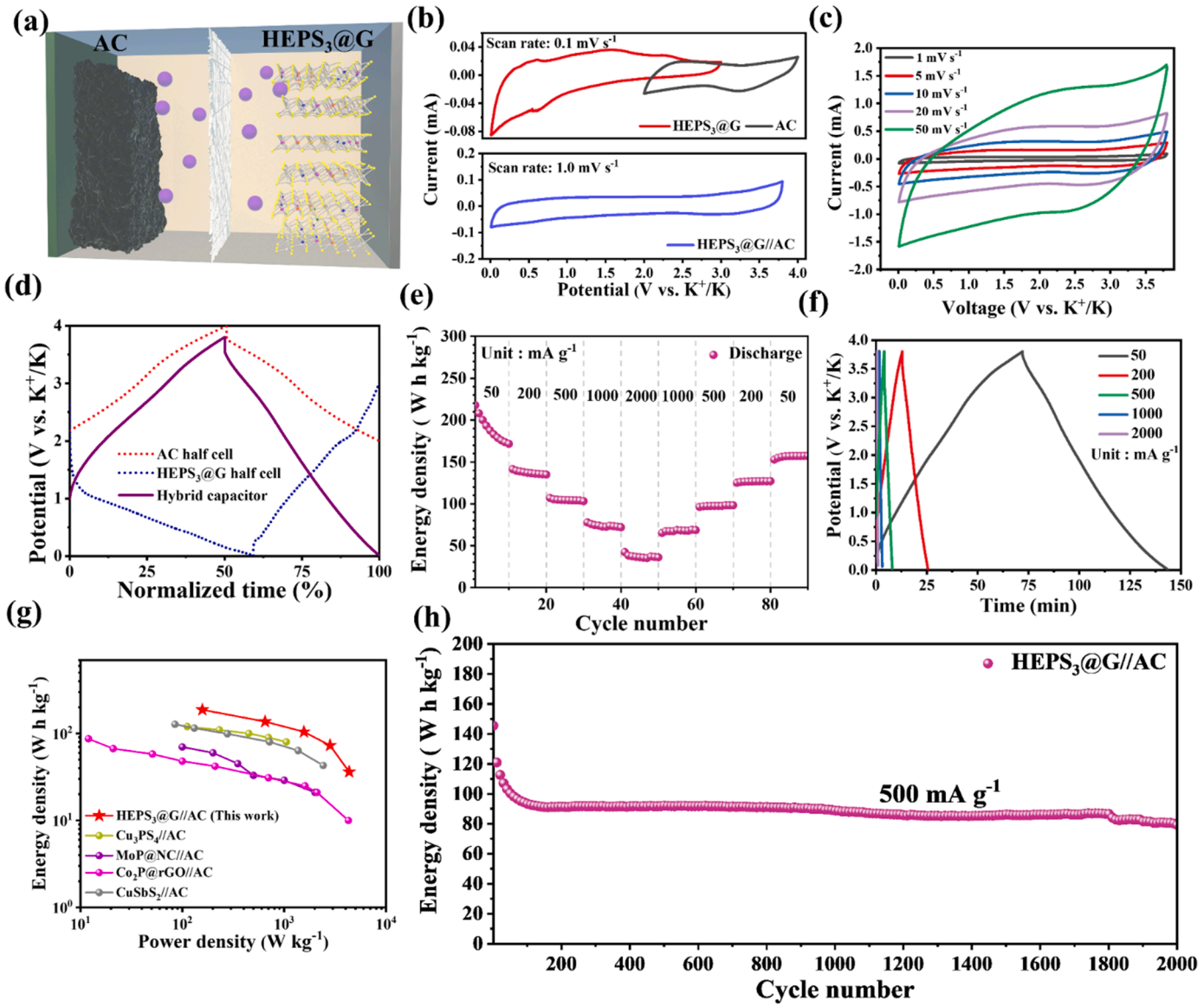

Fig. 11. Hybrid capacitor of $HEPS_3$@G//AC. (a) Schematic diagram of a $HEPS_3$@G//AC hybrid capacitor. (b) CV curves of AC half cell, $HEPS_3$@G half cell and $HEPS_3$@G//AC hybrid capacitor. (c) CV curves at various scan rates and (d) normalized GCD curves of the PIHC. (e) Rate performance at the current densities from 50 to 2000 mA g^{-1}, and (f) the normalized GCD curves plotted corresponded to rate capability. (g) Ragone plot of the $HEPS_3$@G//AC coin type hybrid capacitor in comparison with the reported PIHCs. (h) Long-term cycling performance of the $HEPS_3$@G//AC PIHC at 500 mA g^{-1}.

Our subsequent studies demonstrate the practical application of PIBs and PIHCs employing $HEPS_3$@G as an anode. Prussian blue (PB) was selected as the cathode because it has a high operating voltage that can accommodate the high oxidation potential of the conversion product K_2S. The half-cell assembly of PB has a stable capacity of 63 mAh g^{-1} (Fig. S36). The schematic diagram of the K^+ full battery system is shown in Fig. 10a. The CV curve of the $HEPS_3$@G//PB full battery (Fig. 10b) shows an anode peak at 3.65 V in the first charging cycle, indicating an oxidation reaction and the formation of a SEI film. The CV curves are well-overlapped after the second cycle, indicating high reversibility of the chemical reaction. Two pairs of redox peaks can be identified at 2.5/3.14 and 3.11/3.38 V. Fig. 10c shows the typical GCD profiles of the $HEPS_3$@G half-cell, PB half-cell, and $HEPS_3$@G//PB full cell at a current density of 50 mA g^{-1}. The initial charge and discharge capacities of the full cell are 373.55 mAh g^{-1} and 353.55 mAh g^{-1}, respectively, and the plateaus are consistent with the CV curve results. Fig. 10d shows the GCD curves at various current densities, and the $HEPS_3$@G//PB full cell still exhibits excellent rate performance despite a slight overpotential shift at high current densities. Long-term cycle tests at current densities of 50 mA g^{-1} (Fig. 10e) and 300 mA g^{-1} (Fig. 10g) show that the $HEPS_3$@G//PB full cell can deliver reversible capacity of 450 mAh g^{-1} for 50 cycles. The full cell of PIBs maintain a reversible capacity of 300 mAh g^{-1} for 300 cycles, which is similar to that of the $HEPS_3$@G half cell.

Furthermore, we assembled a PIHC asymmetric device ($HEPS_3$@G//AC), which consists of a $HEPS_3$@G anode and a commercial activated carbon (AC) cathode, to demonstrate the advantages of high-entropy materials in terms of electron and K^+ transfer. Due to the fast diffusion ability and excellent kinetic properties of K^+ in the metal phosphorus trichalcogendies nanosheets with high entropy, FSI ions in the electrolyte can pass through the EDLC on the surface of the anode by adsorption and desorption, leading to high energy density [61]. The working voltage was set in the range of 0.01 V-3.8 V to achieve high energy and high power density. The schematic diagram of the K^+ hybrid capacitor system is shown in Fig. 11a. The CV curves of the successfully assembled PIHCs exhibit typical capacitive behavior (Fig. 11b), which

proves that the $HEPS_3$@G//AC hybrid capacitor has no side reactions in this voltage range. Fig. 11c shows the CV curves measured at different scan rates of 1.0, 5.0, 10, 20, and 50 mV s^{-1}. The kinetic analysis of the CV curves at high rates reveals that the proportional increase in peak capacitance has no apparent overpotential shift, indicating that pseudocapacitance is highly dominant in the PIHC device. The corresponding GCD curve with a straight line (Fig. 11d) is also provided and is typical of hybrid capacitor behavior, contributing to good rate performance. Fig. 11e shows the rate capability of the $HEPS_3$@G//AC based on the total mass of $HEPS_3$@G and AC, achieving energy densities of 187.53, 136.98, 104.49, 72.86, and 36.18 Wh Kg^{-1} at current densities of 50, 200, 500, 1000, and 2000 mA g^{-1}, respectively. When the current density was restored to 200 mA g^{-1}, the energy density still reached 127.09 $WhKg^{-1}$, demonstrating its exceptional reversibility. Notably, the GCD curves of the $HEPS_3$@G//AC at various current densities (Fig. 11f) show that the high energy density of 187.53 Wh Kg^{-1} can be maintained at a current density of 50 mA g^{-1} for over 140 s, significantly higher than most reported K^+ hybrid capacitors.

The advantages of the novel capacitor were evaluated by plotting the energy and power densities of sulfur and phosphorus compounds in the Ragone diagram (Fig. 11g). The $HEPS_3$@G//AC PIHC outperforms other materials, including Cu_3PS_4//AC [62], MoP@NC//AC [63], Co_2P@r-GO//AC [64], and $CuSbS_2$//AC [65], in terms of energy and power density. Importantly, the long-term cycling performance of the PIHC achieved an energy density of 100 Wh Kg^{-1} at a high current density of 500 mA g^{-1} (Fig. 11g) and still maintained a retention rate of 74.6% after 2000 cycles. The excellent performance of the $HEPS_3$@G//AC hybrid capacitor is attributed to the sufficient active sites in the $HEPS_3$, proper adsorption, and high reversible capacity in the faradaic process.

4. Conclusion

In summary, the concepts of high entropy and two-dimensional materials have been integrated in the application of potassium-ion storage devices, where doped elements are uniformly distributed at the nano and micron scale to facilitate efficient potassium-ion transport. A comparison of five $MPCH_3$-type systems with different configurational entropies reveals the sources of their performance enhancements related to the high-entropy effect. The unique plate-like structural features composed of in situ formed alloy not only promote enhanced conversion of polysulfides but also strongly capture K_2S to suppress the common "shuttle effect" in sulfide materials. Furthermore, the "lattice distortion effect" in high-entropy materials evenly disperses the internal stress generated in the electrode during the K^+ insertion/extraction process, thereby inhibiting electrode pulverization and improving reversible potassium storage performance. Due to these advantages, the prepared potassium-ion battery with $HEPS_3$@G anode exhibits a remarkable high reversible capacity of 524 mAh g^{-1} and rate performance (10 A g^{-1}). This high-entropy design strategy, combining unique structural benefits and a harmony of various metal structures, provides a solution to the reversibility and cycling challenges faced by conversion-type sulfide anode materials and demonstrates the immense potential for practical potassium-ion battery applications.

CRediT authorship contribution statement

Po-Wen Chien: Conceptualization, Methodology, Data curation. **Che-Bin Chang:** Data curation. **Hsing-Yu Tuan:** Conceptualization, Resources, Supervision, Writing – review & editing.

Declaration of Competing Interest

The authors declare that they have no known competing financial interests or personal relationships that could have appeared to influence the work reported in this paper.

Data availability

Data will be made available on request.

Acknowledgement

This work received financial support from the 2030 Cross-Generation Young Scholars Program by National Science and Technology Council, Taiwan (NSTC 112–2628-E-007–010). H.-Y. Tuan also acknowledges the financial support of National Tsing Hua University, Taiwan, through Grant No. 112B0011J2. The authors thank Ms. Y. M. Chang (Instrumentation center at NTHU) for Spherical-aberration Corrected Field Emission TEM analysis.

Supplementary materials

Supplementary material associated with this article can be found, in the online version, at doi:10.1016/j.ensm.2023.102853.

References

[1] L. Sun, G. Li, S. Zhang, S. Liu, J. Yuwono, J. Mao, Z. Guo, Practical assessment of the energy density of potassium-ion batteries, Sci. China Chem. (2022) 1–9, https://doi.org/10.1007/s11426-022-1442-4.
[2] X. Yu, X. Ren, Z. Yuan, X. Hou, T. Yang, M. Wang, Ni_3S_2–Ni Hybrid Nanospheres with Intra-Core Void Structure Encapsulated in N-Doped Carbon Shells for Efficient and Stable K-ion Storage, Adv. Sci. 10 (2023), 2205556, https://doi.org/10.1002/advs.202205556.
[3] K. Qin, K. Holguin, J. Huang, M. Mohammadiroudbari, F. Chen, Z. Yang, G.L. Xu, C. Luo, A Fast-Charging and High-Temperature All-Organic Rechargeable Potassium Battery, Adv. Sci. 9 (2022), 2106116, https://doi.org/10.1002/advs.202106116.
[4] J. Liao, C. Chen, Q. Hu, Y. Du, Y. He, Y. Xu, Z. Zhang, X. Zhou, A low-strain phosphate cathode for high-rate and ultralong cycle-life potassium-ion batteries, Angew. Chem. 133 (2021) 25779–25786, https://doi.org/10.1002/ange.202112183.
[5] C. Wei, Y. Tao, H. Fei, Y. An, Y. Tian, J. Feng, Y. Qian, Recent advances and perspectives in stable and dendrite-free potassium metal anodes, Energy Stor. Mater. 30 (2020) 206–227, https://doi.org/10.1016/j.ensm.2020.05.018.
[6] M. Shen, H. Ding, L. Fan, A.M. Rao, J. Zhou, B. Lu, Neuromorphic Carbon for Fast and Durable Potassium Storage, Adv. Funct. Mater. (2023), 2213362, https://doi.org/10.1002/adfm.202213362.
[7] C. Ma, X. Tang, J. Jiang, Z. Ma, H. Li, H. Ben, X.-Z. Yuan, Constructing sulfur and nitrogen codoped porous carbon with optimized defect-sites and electronic structure promises high performance potassium-ion storage, Chem. Eng. J. 454 (2023), 140116, https://doi.org/10.1016/j.cej.2022.140116.
[8] K.-T. Chen, S. Chong, L. Yuan, Y.-C. Yang, H.-Y. Tuan, Conversion-alloying dual mechanism anode: nitrogen-doped carbon-coated Bi_2Se_3 wrapped with graphene for superior potassium-ion storage, Energy Stor. Mater. 39 (2021) 239–249, https://doi.org/10.1016/j.ensm.2021.04.019.
[9] P. Xiong, J. Wu, M. Zhou, Y. Xu, Bismuth–antimony alloy nanoparticle@ porous carbon nanosheet composite anode for high-performance potassium-ion batteries, ACS Nano 14 (2019) 1018–1026, https://doi.org/10.1021/acsnano.9b08526.
[10] D. Li, X. Ren, Q. Ai, Q. Sun, L. Zhu, Y. Liu, Z. Liang, R. Peng, P. Si, J. Lou, Facile fabrication of nitrogen-doped porous carbon as superior anode material for potassium-ion batteries, Adv. Energy Mater. 8 (2018), 1802386, https://doi.org/10.1002/aenm.201802386.
[11] Y.-Y. Hsieh, K.-T. Chen, H.-Y. Tuan, A synergetic SnSb-amorphous carbon composites prepared from polyesterification process as an ultrastable potassium-ion battery anode, Chem. Eng. J. 420 (2021), 130451, https://doi.org/10.1016/j.cej.2021.130451.
[12] D. Zhang, J. Lu, C. Pei, S. Ni, Electrochemical activation, sintering, and reconstruction in energy-storage technologies: origin, development, and prospects, Adv. Energy Mater. 12 (2022), 2103689, https://doi.org/10.1002/aenm.202103689.
[13] F. Wang, H.-C. Yu, M.-H. Chen, L. Wu, N. Pereira, K. Thornton, A. Van der Ven, Y. Zhu, G.G. Amatucci, J. Graetz, Tracking lithium transport and electrochemical reactions in nanoparticles, Nat. Commun. 3 (2012) 1201, https://doi.org/10.1038/ncomms2185.
[14] M. Wu, W. Zheng, X. Hu, F. Zhan, Q. He, H. Wang, Q. Zhang, L. Chen, Exploring 2D Energy Storage Materials: advances in Structure, Synthesis, Optimization Strategies, and Applications for Monovalent and Multivalent Metal-Ion Hybrid Capacitors, Small 18 (2022), 2205101, https://doi.org/10.1002/smll.202205101.
[15] J. Wan, S.D. Lacey, J. Dai, W. Bao, M.S. Fuhrer, L. Hu, Tuning two-dimensional nanomaterials by intercalation: materials, properties and applications, Chem. Soc. Rev. 45 (2016) 6742–6765, https://doi.org/10.1039/C5CS00758E.
[16] S. Kandambeth, V.S. Kale, O. Shekhah, H.N. Alshareef, M. Eddaoudi, 2D covalent-organic framework electrodes for supercapacitors and rechargeable metal-ion

batteries, Adv. Energy Mater. 12 (2022), 2100177, https://doi.org/10.1002/aenm.202100177.
[17] X. Yang, Y. Luo, J. Li, H. Wang, Y. Song, J. Li, Z. Guo, Tuning Mixed Electronic/Ionic Conductivity of 2D $CdPS_3$ Nanosheets as an Anode Material by Synergistic Intercalation and Vacancy Engineering, Adv. Funct. Mater. 32 (2022), 2112169, https://doi.org/10.1002/adfm.202112169.
[18] Q. Yun, Y. Ge, B. Chen, L. Li, Q. Wa, H. Long, H. Zhang, Hybridization of 2D nanomaterials with 3D graphene architectures for electrochemical energy storage and conversion, Adv. Funct. Mater. 32 (2022), 2202319, https://doi.org/10.1002/adfm.202202319.
[19] Y. Zhu, L. Peng, Z. Fang, C. Yan, X. Zhang, G. Yu, Structural engineering of 2D nanomaterials for energy storage and catalysis, Adv. Mater. 30 (2018), 1706347, https://doi.org/10.1002/adma.201706347.
[20] G. Anand, J. Gray, E. Siemsen, Decay, shock, and renewal: operational routines and process entropy in the pharmaceutical industry, Organ. Sci. 23 (2012) 1700–1716, https://doi.org/10.1287/orsc.1110.0709.
[21] K. Mori, N. Hashimoto, N. Kamiuchi, H. Yoshida, H. Kobayashi, H. Yamashita, Hydrogen spillover-driven synthesis of high-entropy alloy nanoparticles as a robust catalyst for CO_2 hydrogenation, Nat. Commun. 12 (2021) 3884, https://doi.org/10.1038/s41467-021-24228-z.
[22] B. Jiang, Y. Yu, J. Cui, X. Liu, L. Xie, J. Liao, Q. Zhang, Y. Huang, S. Ning, B. Jia, High-entropy-stabilized chalcogenides with high thermoelectric performance, Science 371 (2021) 830–834, https://doi.org/10.1126/science.abe1292.
[23] L. Su, J. Ren, T. Lu, K. Chen, J. Ouyang, Y. Zhang, X. Zhu, L. Wang, H. Min, W. Luo, Deciphering Structural Origins of Highly Reversible Lithium Storage in High Entropy Oxides with In Situ Transmission Electron Microscopy, Adv. Mater. 35 (2023), 2205751, https://doi.org/10.1002/adma.202205751.
[24] Y. Ma, Y. Ma, Q. Wang, S. Schweidler, M. Botros, T. Fu, H. Hahn, T. Brezesinski, B. Breitung, High-entropy energy materials: challenges and new opportunities, Energy Environ. Sci. 14 (2021) 2883–2905, https://doi.org/10.1039/D1EE00505G.
[25] R. Wang, J. Huang, X. Zhang, J. Han, Z. Zhang, T. Gao, L. Xu, S. Liu, P. Xu, B. Song, Two-dimensional high-entropy metal phosphorus trichalcogenides for enhanced hydrogen evolution reaction, ACS Nano 16 (2022) 3593–3603, https://doi.org/10.1021/acsnano.2c01064.
[26] B. Xiao, G. Wu, T. Wang, Z. Wei, Y. Sui, B. Shen, J. Qi, F. Wei, J. Zheng, High-entropy oxides as advanced anode materials for long-life lithium-ion Batteries, Nano Energy 95 (2022), 106962, https://doi.org/10.1016/j.nanoen.2022.106962.
[27] J. Zhao, Y. Zhang, X. Chen, G. Sun, X. Yang, Y. Zeng, R. Tian, F. Du, Entropy-change driven highly reversible sodium storage for conversion-type sulfide, Adv. Funct. Mater. 32 (2022), 2206531, https://doi.org/10.1002/adfm.202206531.
[28] Z. Yi, J. Xu, Z. Xu, M. Zhang, Y. He, J. Bao, X. Zhou, Ultrafine SnSSe/multilayer graphene nanosheet nanocomposite as a high-performance anode material for potassium-ion half/full batteries, J. Energy Chem. 60 (2021) 241–248, https://doi.org/10.1016/j.jechem.2021.01.022.
[29] L. Ren, J. Liu, Y. Zhao, Y. Wang, X. Lu, M. Zhou, G. Zhang, W. Liu, H. Xu, X. Sun, Regulating electronic structure of Fe–N_4 single atomic catalyst via neighboring sulfur doping for high performance lithium–sulfur batteries, Adv. Funct. Mater. 33 (2023), 2210509, https://doi.org/10.1002/adfm.202210509.
[30] F. Yuan, D. Zhang, Z. Li, H. Sun, Q. Yu, Q. Wang, J. Zhang, Y. Wu, K. Xi, B. Wang, Unraveling the intercorrelation between micro/mesopores and K migration behavior in hard carbon, Small 18 (2022), 2107113, https://doi.org/10.1002/smll.202107113.
[31] Y. Ma, Y. Hu, Y. Pramudya, T. Diemant, Q. Wang, D. Goonetilleke, Y. Tang, B. Zhou, H. Hahn, W. Wenzel, Resolving the role of configurational entropy in improving cycling performance of multicomponent hexacyanoferrate cathodes for sodium-ion batteries, Adv. Funct. Mater. 32 (2022), 2202372, https://doi.org/10.1002/adfm.202202372.
[32] J. Tang, C.-Y. Wang, F. Xiu, A.J. Hong, S. Chen, M. Wang, C. Zeng, H.-J. Yang, H.-Y. Tuan, C.-J. Tsai, Single-crystalline $Ni_2Ge/Ge/Ni_2Ge$ nanowire heterostructure transistors, Nanotechnology 21 (2010), 505704, https://doi.org/10.1088/0957-4484/21/50/505704.
[33] F.-W. Yuan, H.-J. Yang, H.-Y. Tuan, Seeded silicon nanowire growth catalyzed by commercially available bulk metals: broad selection of metal catalysts, superior field emission performance, and versatile nanowire/metal architectures, J. Mater. Chem. 21 (2011) 13793–13800, https://doi.org/10.1039/C1JM11956G.
[34] H.-J. Yang, C.-Y. Chen, F.-W. Yuan, H.-Y. Tuan, Designed synthesis of solid and hollow Cu_2–x Te nanocrystals with tunable near-infrared localized surface plasmon resonance, J. Phys. Chem. C 117 (2013) 21955–21964, https://doi.org/10.1021/jp407559b.
[35] Y. Ma, X. Lian, N. Xu, H. Jiang, L. Li, D. Zhang, G. Hu, S. Peng, Rational design of few-layer $FePS_3$ nanosheets@ N-doped carbon composites as anodes for sodium-ion batteries, Chem. Eng. J. 427 (2022), 130882, https://doi.org/10.1016/j.cej.2021.130882.
[36] W.Y. Chen, A. Yermembetova, B.M. Washer, X. Jiang, S.N. Shuvo, D. Peroulis, A. Wei, L.A. Stanciu, Selective detection of ethylene by MoS_2–carbon nanotube networks coated with Cu (I)–pincer complexes, ACS Sens. 5 (2020) 1699–1706, https://doi.org/10.1021/acssensors.0c00344.
[37] X. Xu, Y. Guo, B.P. Bloom, J. Wei, H. Li, H. Li, Y. Du, Z. Zeng, L. Li, D.H. Waldeck, Elemental core level shift in high entropy alloy nanoparticles via X-ray photoelectron spectroscopy analysis and first-principles calculation, ACS Nano 14 (2020) 17704–17712, https://doi.org/10.1021/acsnano.0c09470.
[38] C.-Y. Tsai, C.-H. Chang, T.-L. Kao, K.-T. Chen, H.-Y. Tuan, Shape matters: $SnP_{0.94}$ teardrop nanorods with boosted performance for potassium ion storage, Chem. Eng. J. 417 (2021), 128552, https://doi.org/10.1016/j.cej.2021.128552.
[39] T.X. Nguyen, C.-C. Tsai, J. Patra, O. Clemens, J.-K. Chang, J.-M. Ting, Co-free high entropy spinel oxide anode with controlled morphology and crystallinity for outstanding charge/discharge performance in Lithium-ion batteries, Chem. Eng. J. 430 (2022), 132658, https://doi.org/10.1016/j.cej.2021.132658.
[40] L. Lin, K. Wang, A. Sarkar, C. Njel, G. Karkera, Q. Wang, R. Azmi, M. Fichtner, H. Hahn, S. Schweidler, High-entropy sulfides as electrode materials for Li-Ion batteries, Adv. Energy Mater. 12 (2022), 2103090, https://doi.org/10.1002/aenm.202103090.
[41] F. Yuan, Z. Li, D. Zhang, Q. Wang, H. Wang, H. Sun, Q. Yu, W. Wang, B. Wang, Fundamental understanding and research progress on the interfacial behaviors for potassium-ion battery anode, Adv. Sci. 9 (2022), 2200683, https://doi.org/10.1002/advs.202200683.
[42] B. Wang, Z. Zhang, F. Yuan, D. Zhang, Q. Wang, W. Li, Z. Li, Y.A. Wu, W. Wang, An insight into the initial Coulombic efficiency of carbon-based anode materials for potassium-ion batteries, Chem. Eng. J. 428 (2022), 131093, https://doi.org/10.1016/j.cej.2021.131093.
[43] W. Tan, F. Yang, T. Yi, G. Liu, X. Wei, Q. Long, Y. Liu, Y. Li, C. Guo, K. Liu, Fullerene-like elastic carbon coatings on silicon nanoparticles by solvent controlled association of natural polyaromatic molecules as high-performance lithium-ion battery anodes, Energy Stor. Mater. 45 (2022) 412–421, https://doi.org/10.1016/j.ensm.2021.11.040.
[44] C. Choi, D. Ashby, Y. Rao, E. Anber, J.L. Hart, D. Butts, C. Wilson, E. Levin, M. Taheri, M. Ghazisaeidi, Mechanistic insight and local structure evolution of $NiPS_3$ upon electrochemical lithiation, ACS Appl. Mater. Interfaces 14 (2022) 3980–3990, https://doi.org/10.1021/acsami.1c19963.
[45] S. Haghighat-Shishavan, M. Nazarian-Samani, M. Nazarian-Samani, K.-B. Kim, Electrolyte modulation of $BiPS_4$ concurrently suppressing the Bi coarsening and polysulfide shuttle effect in K-ion batteries, Energy Stor. Mater. 39 (2021) 96–107, https://doi.org/10.1016/j.ensm.2021.03.037.
[46] D. Cabrera-German, G. Molar-Velázquez, G. Gómez-Sosa, W. De la Cruz, A. Herrera-Gomez, Detailed peak fitting analysis of the Zn 2p photoemission spectrum for metallic films and its initial oxidation stages, Surf. Interface Anal. 49 (2017) 1078–1087, https://doi.org/10.1002/sia.6280.
[47] N. Wang, Y. Wang, Z. Bai, Z. Fang, X. Zhang, Z. Xu, Y. Ding, X. Xu, Y. Du, S. Dou, High-performance room-temperature sodium–sulfur battery enabled by electrocatalytic sodium polysulfides full conversion, Energy Environ. Sci. 13 (2020) 562–570, https://doi.org/10.1039/C9EE03251G.
[48] Z. Zhao, Z. Yi, H. Li, R. Pathak, Z. Yang, X. Wang, Q. Qiao, Synergetic effect of spatially separated dual co-catalyst for accelerating multiple conversion reaction in advanced lithium sulfur batteries, Nano Energy 81 (2021), 105621, https://doi.org/10.1016/j.nanoen.2020.105621.
[49] P. Wang, B. Xi, M. Huang, W. Chen, J. Feng, S. Xiong, Emerging catalysts to promote kinetics of lithium–sulfur batteries, Adv. Energy Mater. 11 (2021), 2002893, https://doi.org/10.1002/aenm.202002893.
[50] Q. Liu, W. Deng, C.-F. Sun, A potassium–tellurium battery, Energy Stor. Mater. 28 (2020) 10–16, https://doi.org/10.1016/j.ensm.2020.02.021.
[51] J. Häcker, D.H. Nguyen, T. Rommel, Z. Zhao-Karger, N. Wagner, K.A. Friedrich, Operando UV/vis spectroscopy providing insights into the sulfur and polysulfide dissolution in magnesium–sulfur batteries, ACS Energy Lett. 7 (2021) 1–9, https://doi.org/10.1021/acsenergylett.1c02152.
[52] X.L. Huang, X. Zhang, L. Zhou, Z. Guo, H.K. Liu, S.X. Dou, Z. Wang, Orthorhombic Nb_2O_5 decorated carbon nanoreactors enable bidirectionally regulated redox behaviors in room-temperature Na–S batteries, Adv. Sci. 10 (2023), 2206558, https://doi.org/10.1002/advs.202206558.
[53] G. Janz, J. Coutts, J. Downey, E. Roduner, Raman studies of sulfur-containing anions in inorganic polysulfides. Potassium polysulfides, Inorg. Chem. 15 (1976) 1755–1759, https://doi.org/10.1021/ic50162a003.
[54] X. Lu, M.E. Bowden, V.L. Sprenkle, J. Liu, A low cost, high energy density, and long cycle life potassium–sulfur battery for grid-scale energy storage, Adv. Mater. 27 (2015) 5915–5922, https://doi.org/10.1002/adma.201502343.
[55] X. Yang, C. Wang, P. Yan, T. Jiao, J. Hao, Y. Jiang, F. Ren, W. Zhang, J. Zheng, Y. Cheng, Pushing lithium cobalt oxides to 4.7V by lattice-matched interfacial engineering, Adv. Energy Mater. 12 (2022), 2200197, https://doi.org/10.1002/aenm.202200197.
[56] G. Yoo, B.-R. Koo, Nano-sized split V_2O_5 with H_2O-intercalated interfaces as a stable cathode for zinc ion batteries without an aging process, Chem. Eng. J. 434 (2022), 134738, https://doi.org/10.1016/j.cej.2022.134738.
[57] S. Zhang, Y. Zhang, Z. Zhang, H. Wang, Y. Cao, B. Zhang, X. Liu, C. Mao, X. Han, H. Gong, Bi Works as a Li reservoir for promoting the fast-charging performance of phosphorus anode for Li-ion batteries, Adv. Energy Mater. 12 (2022), 2103888, https://doi.org/10.1002/aenm.202103888.
[58] X. Ou, T. Liu, W. Zhong, X. Fan, X. Guo, X. Huang, L. Cao, J. Hu, B. Zhang, Y. S. Chu, Enabling high energy lithium metal batteries via single-crystal Ni-rich cathode material co-doping strategy, Nat. Commun. 13 (2022) 2319, https://doi.org/10.1038/s41467-022-30020-4.
[59] Y. Lu, T. Zhu, E. McShane, B.D. McCloskey, G. Chen, Single-crystal $LiNixMnyCo_{1-x-y}O_2$ cathodes for extreme fast charging, Small 18 (2022), 2105833, https://doi.org/10.1002/smll.202105833.
[60] W. Zhao, L. Zou, L. Zhang, X. Fan, H. Zhang, F. Pagani, E. Brack, L. Seidl, X. Ou, K. Egorov, Assessing long-term cycling stability of single-crystal versus polycrystalline nickel-rich NCM in pouch cells with 6 mAh cm^{-2} electrodes, Small 18 (2022), 2107357, https://doi.org/10.1002/smll.202107357.
[61] C.-H. Chang, K.-T. Chen, Y.-Y. Hsieh, C.-B. Chang, H.-Y. Tuan, Crystal facet and architecture engineering of metal oxide nanonetwork anodes for high-performance potassium ion batteries and hybrid capacitors, ACS Nano 16 (2022) 1486–1501, https://doi.org/10.1021/acsnano.1c09863.

[62] S.-F. Ho, H.-Y. Tuan, Cu_3PS_4: a sulfur-rich metal phosphosulfide with superior ionic diffusion channel for high-performance potassium ion batteries/hybrid capacitors, Chem. Eng. J. 452 (2023), 139199, https://doi.org/10.1016/j.cej.2022.139199.
[63] W. Zong, N. Chui, Z. Tian, Y. Li, C. Yang, D. Rao, W. Wang, J. Huang, J. Wang, F. Lai, Ultrafine MoP nanoparticle splotched nitrogen-doped carbon nanosheets enabling high-performance 3D-printed potassium-ion hybrid capacitors, Adv. Sci. 8 (2021), 2004142, https://doi.org/10.1002/advs.202004142.
[64] Y. Wang, Z. Zhang, G. Wang, X. Yang, Y. Sui, F. Du, B. Zou, Ultrafine Co_2P nanorods wrapped by graphene enable a long cycle life performance for a hybrid potassium-ion capacitor, Nanoscale Horiz. 4 (2019) 1394–1401, https://doi.org/10.1039/C9NH00211A.
[65] C.-B. Chang, K.-T. Chen, H.-Y. Tuan, Large-scale synthesis of few-layered copper antimony sulfide nanosheets as electrode materials for high-rate potassium-ion storage, J. Colloid Interface Sci. 608 (2022) 984–994, https://doi.org/10.1016/j.jcis.2021.09.154.